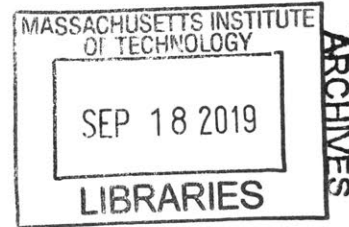A GLOBAL STUDY OF DOUBLE SEISMIC ZONES AND ITS IMPLICATIONS FOR THE MECHANISM OF INTERMEDIATE-DEPTH EARTHQUAKES

By

Manuel A. Florez Torres

M.S. Physics
Universidad de Los Andes, Bogotá, Colombia

SUBMITTED TO THE DEPARTMENT OF EARTH, ATMOSPHERIC AND PLANETARY SCIENCES IN PARTIAL FULFILLMENT OF THE REQUIREMENTS FOR THE DEGREE OF

DOCTOR OF PHILOSOPHY
AT THE
MASSACHUSETTS INSTITUTE OF TECHNOLOGY

SEPTEMBER, 2019

Signature redacted

Signature of Author: _____
Department of Earth, Atmospheric and Planetary Science
August 30, 2019

Signature redacted

Certified by _____
German A. Prieto
Associate Professor
Thesis supervisor

Signature redacted

Accepted by:_____ _____
Robert D. van der Hilst
Schlumberger Professor of Earth Sciences
Head of Department of Earth, Atmospheric and Planetary Sciences

A global Study of Double Seismic Zones and its Implications for the
Mechanism of Intermediate-Depth Earthquakes

By
Manuel A. Florez Torres

Submitted to the Department of Earth, Atmospheric, and Planetary Sciences
On August 30, 2019, in partial fulfillment of the
requirements for the degree of
Doctor of Philosophy in Geophysics

Abstract

The fundamental physical processes to generate earthquakes contradict the occurrence of intermediate-depth (80-350 km) seismicity: both pressure and temperature increase with depth, which inhibits fracture, unstable sliding, and promotes ductile flow. Classic experiments on olivine, the main mineral that composes the mantle, show that the shear stresses necessary to overcome the high normal stresses imposed by the overburden pressure are unsustainable at these depths. In subduction zones, the dehydration of the descending oceanic lithosphere might enable the observed brittle-like behavior; but this hypothesis remains controversial, as there are other viable alternatives. Improving our understanding of the intermediate-depth seismicity relies on assembling accurate and systematic seismological observations, which I tackle here in my graduate work.

First, I developed a relocation method that uses array processing in such a way that velocity model biases are reduced. The technique identifies and picks the arrival of depth phases and perform a relative relocation scheme. When high-quality data is available, hypocentral depth can be estimated with a precision of a few kilometers. I systematically applied this technique to build a new global catalog of intermediate depth seismicity.

At depths larger than about 50 km, most subducting slabs feature two distinct layers of seismicity, known as Double Seismic Zones (DSZ). I used my relocated catalog to characterize 32 slab segments, sampling a diverse range of tectonic environments. I was able to clearly resolve the geometrical structure of DSZs and to separately study subducting crust (upper layer) and lithospheric mantle (lower layer) earthquakes. I performed a careful analysis of the frequency-size statistics for each layer, finding consistently larger b-values (proportion of low-to-high magnitude events), correlating with slab age, for the upper plane of the lithosphere while a roughly constant values for the lower plane. Provided that b-values are indicative of stress regime, this suggests a different mechanism for earthquakes happening in the upper and in the lower plan of the subducting oceanic lithosphere.

Thesis supervisor: German A. Prieto

Title: Associate Professor

Dedicada a mi amada esposa Deisy, a mi Papa, a mi
Mama a mi Abuelita Rita y a Carmelita

Acknowledgment

My Ph.D. life at MIT is finally coming to an end, and I have to say thanks to my advisor German A. Prieto, for his patience, guidance and support. A great professor is not who shows us all the knowledge, is who recognizes and respect our ideas and helps us in their development. Thanks German! I am grateful to Prof. Marine Denolle of Harvard University, who provided the encouragement to make this dissertation and the publication of my papers possible. Her feedback and for enlightening discussions improved the rigor of my research. I was very fortunate to work with her. I also thank Rob, Taylor and Brad for all their patience, support and encouragement.

Finally, and certainly not least, I would like to thank my family: my mother who is present every day in my heart, she watches me from heaven, she is my force. My Father for his love and encouragement, my brother, grandmother, aunts, and uncles for their unconditional support and my sweet wife Deisy for her love and patience during this time.

Contents

List of figures

9

lines represent the cuts for profiles A-A' and B-B'. The moment tensor solution for the mainshock is also shown **(b)** Cross section perpendicular to the steeply dipping nodal plane, the red line is the projection of the corresponding steeply dipping plane, catalog locations are shown. **(c)** Same cross section as in panel (b), however the set of events is plotted using our best fitting relative depths. **(d)** Cross section perpendicular to the shallow-dipping nodal plane, the red line is the projection of the corresponding shallow-dipping plane, the black dashed line is the projection of the steeply dipping nodal plane, catalog locations are shown. **(e)** Same cross section as in panel (d), however the set of events is plotted using our best fitting relative depths. 49

Figure 21. Error bars for measurements of the pP-P times at the 12 subarrays shown in Figure 14. The M 5.6 event, in red, ruptured in November 10, 2014 (latitude = $-21.63o$, longitude = $-68.72o$). The M 5.5 earthquake, in black, happened in December 4, 2008 (latitude = $-21.35o$, longitude = $-68.25o$). Both events were included in the relocation example discussed in section 3.1... 53

Figure 22. Error bars for all events in the Double Seismic Zone of the Northern segment of the Nazca plate... 55

Figure 23. Error bars for a set of 17 aftershocks of the M 7.9 Rat Islands archipelago, intermediate depth earthquake. A cross section perpendicular to the steeply dipping nodal plane is plotted, A-A' in Figure 20. The star corresponds to the GCMT centroid of the main shock.. 56

Figure 24. Global map view of major subduction zones with depth contours (orange lines) that follow the Slab1.0 model (Hayes et al., 2012). Arrows represent the segments analyzed, point in the direction of relative plate motion and are color-coded by age. Vertical cross-sections display the improved locations (red dots) and are drawn at the same scale. At each segment analyzed a DSZ was observed, making this pattern of seismicity a global feature as first proposed by Brudzinski et al. (2007).. 60

Figure 25. Estimation of DSZ width and maximum depth-extend (star) and separation of USL and LSL seismicity (red and black circles) for three segments. **(a)** For the relocated catalog in northern Chile, a smoothing spline is used for fitting the upper and lower seismicity (red and black lines respectively). The maximum DSZ depth or merging depth is defined at the merging point of the two spline curves, and the DSZ width is based on the separation between the upper and lower spline curves. For each slab segment, seismicity is separated in USL and LSL according to the distance to either the upper or lower spline curves. In the case where an earthquake is at a similar distance to either spline, it is undetermined whether it belongs to the USL or LSL (empty circle). **(b)** Similar to (a), for the central America DSZ. **(c)** Similar to (a) for the Japan DSZ. **(d)** Similar to (a) for the Marianas DSZ.. 64

List of tables

13

Chapter 1

1. Introduction

1.1 Global Distribution of Seismicity

The global distribution of earthquakes with depth is multimodal (Frohlich, 2006). It falls roughly exponentially from ~70 to ~300 km, remains at a low level until ~500 km, and then shows a marked resurgence before abruptly terminating near 700 km (Figure 1). Surprisingly, only 2.2% of the total number of events reported in the International Seismological Centre (ISC) catalog occurs in the quiet interval between about 350 km and 550 km. A similar distribution of seismicity is observed in every subduction zone (Helffrich and Brodholt, 1991). It is common (Frohlich, 2006 to classify earthquakes by their depth, in three categories: shallow (0-70 km), intermediate-depth (70-300 km) and deep (300-700 km) earthquakes.

In Figure 2 epicenters are color-coded using this classification. Note how most of the earthquakes cluster around subduction zones, which are convergent plate boundaries in which the incoming oceanic plate is subducted beneath an older continental plate. The depth boundaries between categories are approximate, they probably vary among regions.
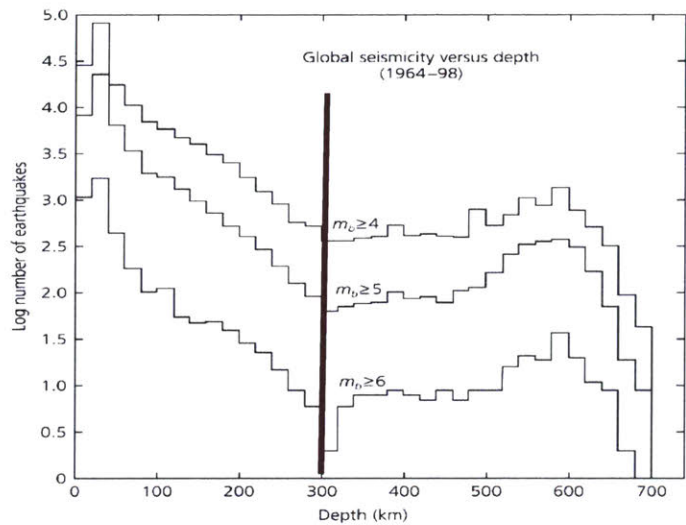
Figure 1. Global distribution of earthquakes as a function of depth. Red line marks the change in slope at about 300 km depth, that is often used as the limit between intermediate-depth and deep earthquakes. Adapted from Stein and Wysession (2003).
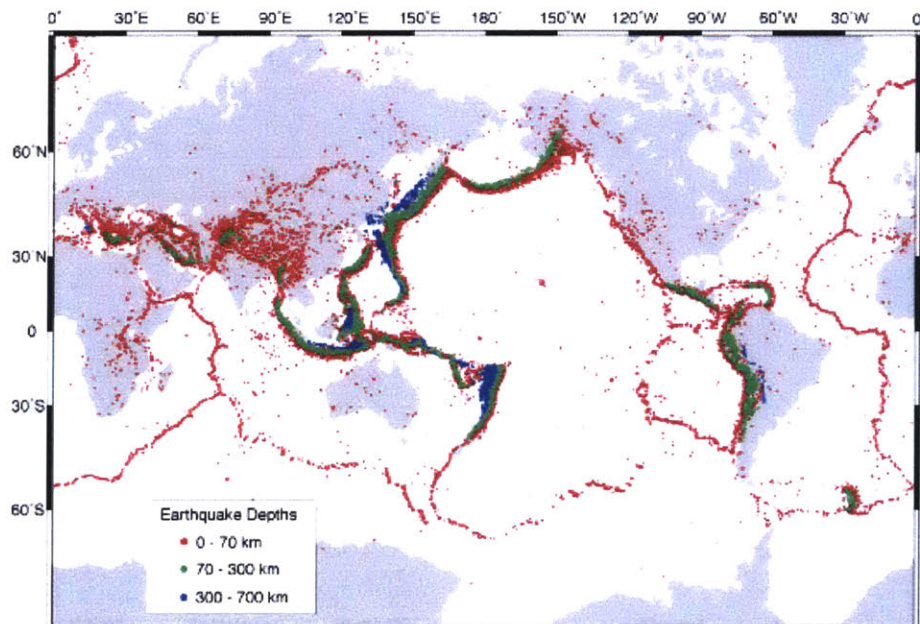
Figure 2. Map view of global seismicity pattern, each point is color coded by category. Adapted from Stein and Wysession (2003).

1.2. Double Seismic Zones

Intermediate-depth earthquakes in subducting slabs cluster in two distinct planes of seismicity along the subducting slab known as Double Seismic Zones (DSZ). Figure 3 bears immense historical importance as it shows the first DSZ discovered in Northeast Honshu, Japan (Hasegawa, 1979), it also clearly depicts two planes of seismicity: An Upper Seismic Layer (USL) and a Lower Seismic Layer (LSL). The gap between them exhibits little to no seismicity.

The aseismic gap in a double seismic zone is of the order of tens of kilometers or less. When compared with this length scale typical location errors in global seismicity catalogs can be significant. Hypocentral depths are particularly problematic, most event locations in global catalog have well constrained epicenter, due to good azimuthal coverage of stations, but lack good vertical resolution (Engdahl et al., 1998). In global catalogs of earthquake locations, the DSZ often exhibit an elongated feature of scattered earthquake locations with various distributions (Figure 4). Global and automated catalogs suffer from poor depth accuracy and resolution, and thus it is often not possible to determine whether an individual event happened in the upper or lower plane. In spite of this limitation, the pioneering work of Brudzinski et al (2007) has stablished that such catalogs are sufficient to statistically determine the presence of the DSZ and compute a rough estimate of its width that marks the average separation between the two seismicity planes.

Brudzinski et al. (2007) analyzes 30 slab segments, sampling a wide range of subduction environments around the world. The presence a DSZ in each segment is assessed by projecting the locations into a 2D coordinate system oriented along the slab dip direction, then simply constructing a histogram to determine whether or not the distributions follows

16

bimodal gaussian distribution. Upon success, the width of the DSZ is simply estimated as the distance between the Gaussian peaks. However, global catalogs suffer from poor depth estimates so that an improved characterization of the geometry and seismicity pattern of the DSZ would require at least one of the following strategies: 1) a use current seismic data to improve hypocentral (and particularly depth) locations and 2) collect new data from local deployments of seismic station located just atop of the segments of interest. The later would be desirable, but much more exhaustive. Instead, this thesis focuses on the first approach.

The gap in seismicity in a DSZ is of the order of tens of kilometers or less. When compared with this length scale typical location errors in global seismicity catalogs can be significant. Hypocentral depth is particularly problematic, most event locations in global catalog have well constrained epicenter, due to good azimuthal coverage, but lack vertical resolution (Engdahl et al., 1998). In spite of this limitation pioneering work has stablished that such catalogs are sufficient to statistically determine the presence of a double seismic zone (Brudzinski et al., 2007). It is important to note that a few local networks have good sampling of slabs with DSZs (Kita et al., 2010; Rietbrock and Waldhauser, 2004) and can be used to assess the reliability of our results.
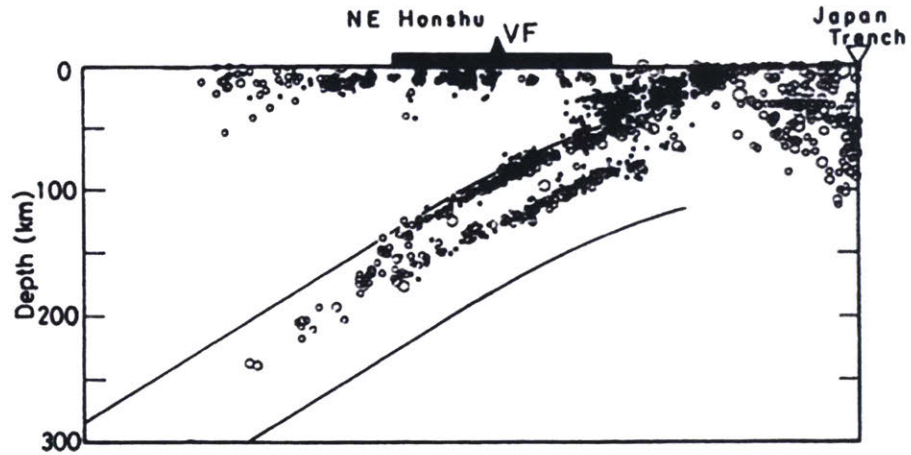
Figure 3. First Double Seismic Zone discovered in Northeast Honshu, Japan. Adapted from Hasegawa, 1979.
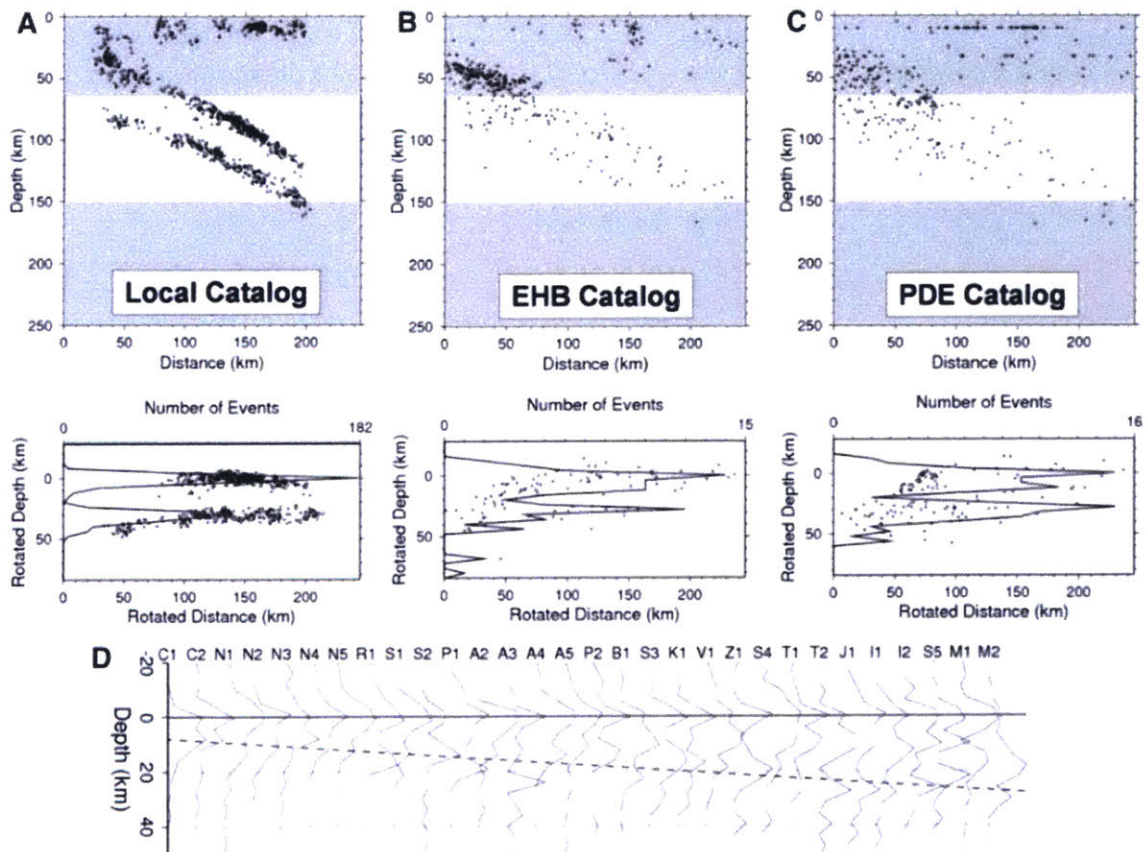
Figure 4. Global prevalence of DSZs and correlation between slab age and DSZ width. Adapted from Brudzinski et. al, 2007.
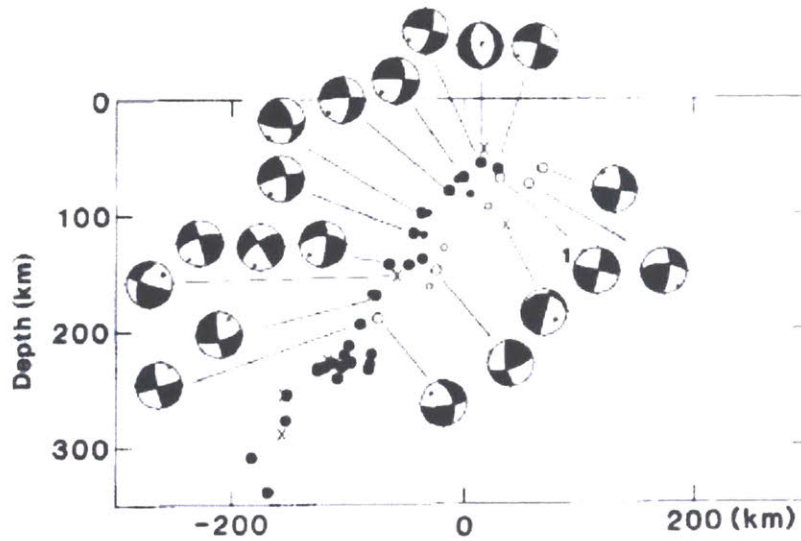
Figure 5. DSZ beneath the Tonga arc. The focal mechanisms of the USL earthquakes show a downdip compressional stress regime, in contrast the ones from the LSL earthquakes are consistent with a downdip extensional regime (Kawakatsu, 1985).
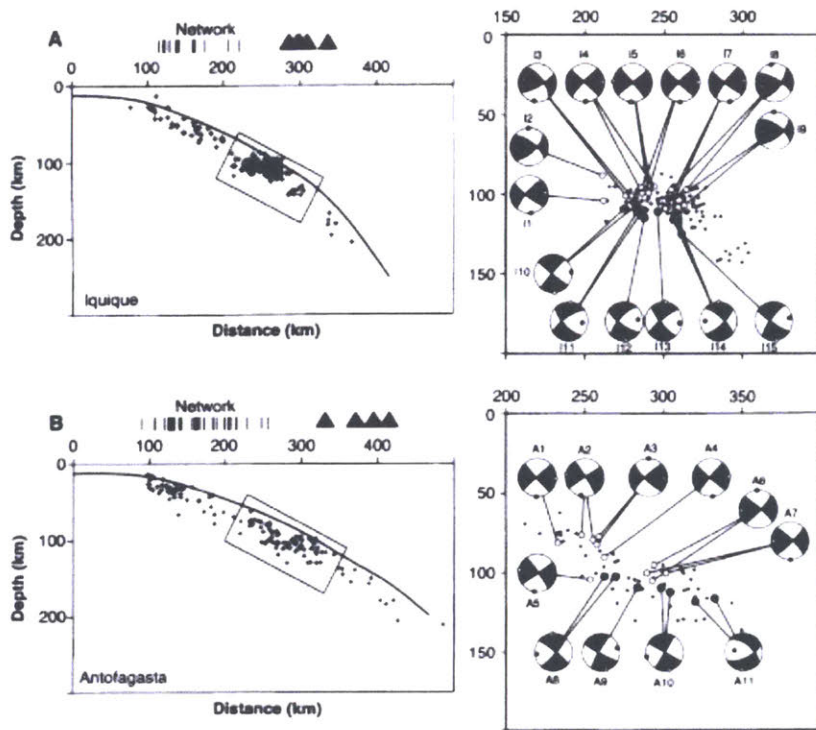
Figure 6. DSZ in Central Chile with a distribution of stresses of opposite polarity relative to the one observed in Japan and Tonga. Adapted from Comte and Suarez, 1994.

19
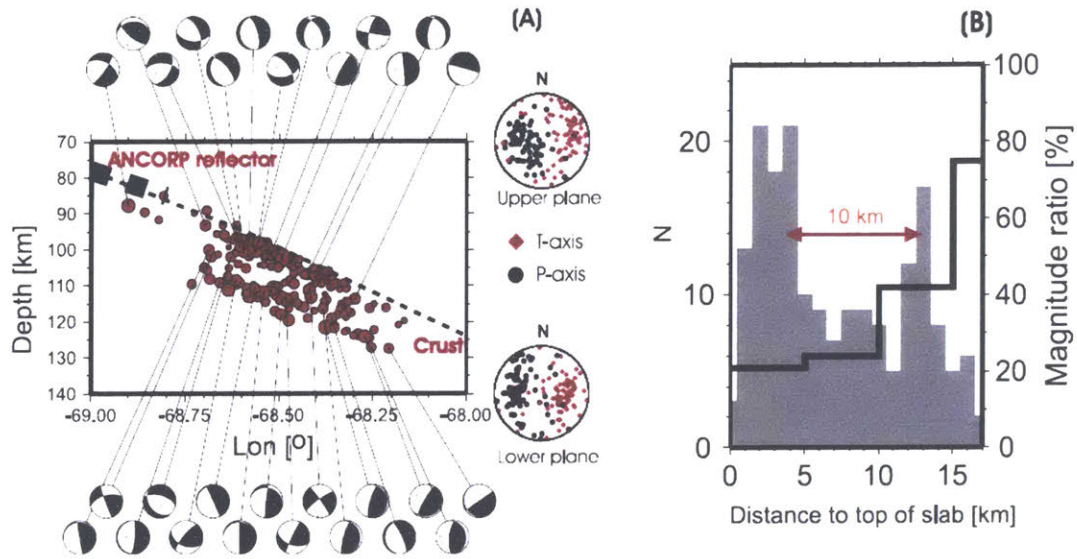
Figure 7. DSZ in Northern Chile resolved using a double difference earthquake relocation and a dense local seismicity catalog. Both layers are consistent with a downdip extensional regime. Adapted from Rietbrock and Waldhauser (2004).

1.3. Physical Mechanism of Intermediate-Depth Seismicity

The fundamental physical processes responsible for the occurrence of intermediate and deep earthquakes are not well understood. Pressure increases with depth and tends to inhibit rapid fracture and seismic sliding. Temperature increases as well, promoting ductile flow (Griggs and Handin, 1960). Furthermore, classic deformation experiments on olivine, the main phase that compose the mantle, show that the shear stresses necessary to overcome the high normal are far greater than anything that can be sustained at the temperatures and pressures consistent with those depths (Brace and Kohlstedt, 1980). Understanding the brittle-frictional processes that yield seismic sliding remains an outstanding challenge that requires integration of seismological, laboratory, and modeling efforts.

In the following we describe the two most widely accepted mechanisms that are proposed to explain the generation of intermediate-depth earthquakes: thermal shear runaway and dehydration embrittlement. This thesis will promote the latter as the most viable mechanism. There is a third mechanism that can operate at great depths, known as metastable phase transition (Green and Houston, 1995; Stein et al., 1996; Frohlich, 2006), which invokes a faulting due to the rapid change in density (volume) of minerals such as olivine, only possible at T-P conditions consistent with depths between 300 km and 550 km. Therefore, it is probably not relevant at intermediate depths (50 – 300 km) and will not be discussed in this thesis.

1.4. Dehydration Embrittlement

Hydrated minerals (e.g., antigorite, chlorite, lawsonite) in the subducting slab undergo phase changes to anhydrous forms, releasing fluids in the process, likely increasing pore pressure, and thus, reducing the effective normal stress necessary to attain brittle failure (Frohlich, 1989; Green and Houston, 1995; Kirby, Stein et al., 1996a; Kirby, Engdahl et al., 1996b; Hacker, Peacock et al., 2003). Experimental results from Rayleigh and Paterson (1965) showed for the first time the viability of this mechanism: the partial dehydration of serpentinite at 700°C and 0.5 GPa, consistent with slab depths of about 100 km, caused weakening and embrittlement of the samples. A plethora of subsequent experiments at different pressures and temperatures confirmed that dehydration embrittlement can operate if fluids are present (Meade and Jeanloz, 1991; Jung, Green et al., 2004; Chollet et al., 2009).

Subducting slabs are naturally hydrated by the oceans. Oceanic crust is pervasively hydrated at mid-ocean ridges, while oceanic lithosphere may be hydrated by fluid transport along outer-rise normal faults (Peacock, 2001). Fluid may be stored in pores, or in mineral phases, and gets released by either squeezing of the pores or various metamorphic phase transitions (Davies, 1999).

Hacker et al. (2003) compared the spatial distribution of intermediate-depth seismicity for four subduction zones: Cascadia, Nankai, Costa Rica, and Tohoku. They inferred locations of hydrous minerals and of the distribution in water content from models of thermal structure and assuming the slab age. They propose that the distribution of the seismicity is consistent with the predicted distribution of several hydrous phases. In the coldest/oldest zone, Tohoku, double planes of seismicity surround the cold core of the slab (Figure 3). Antigorite serpentinite is the most stable hydrous phase is the main component in cooler slabs at intermediate depths and is believed to dehydrate progressively down to about 200 km. Yamasaki and Seno (2003) obtained a similar result analyzing DSZ in six different subduction zones. The combination of a detailed mineralogical model with precisely relocated seismicity provides evidence to date in favor of a dehydration embrittlement mechanism.
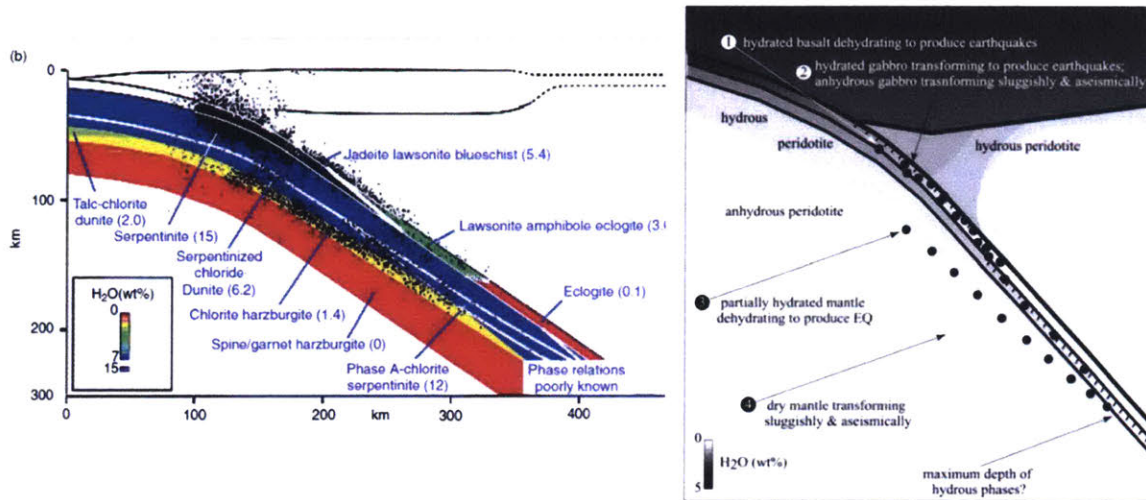
Figure 8. **(a)** Comparison of petrology predicted by thermal structure with hypocentral relocations. The lower zone of a well-developed DSZ follows the predicted locations of regions of serpentinite. (b) Degree of hydration of different model rocks. Adapted from Hacker et al. (2003).

1.5. Dehydration-driven stress transfer

As described in section 1.6 in the dehydration-embrittlement model (Thielmann, 2018; Ferrand et al., 2017) the shear instability develops as the result of fluid overpressure, which reduces the effective confining stress and thus facilitates failure. However, recent work suggests that failure driven by overpressure is only possible if abundant fluids are present (Reynard et al., 2010; Thielmann, 2018), this condition is unlikely to be met in parts of the subducting slab, specially below the oceanic Moho. Furthermore, under typical pressure condition in the lithospheric mantle (1.5-5 GPa) dehydration reactions induce a negative volume change (solid + fluid), which is inconsistent with fluid overpressure (Reynard et al., 2010; Thielmann, 2018). In summary, dehydration embrittlement does not

23

explain seismicity in the lower seismic layer, here we describe an alternative model, the dehydration-driven stress transfer (DDST) recently proposed by Ferrand et al. (2017).

Dehydration-driven stress transfer triggers earthquakes in mantle rocks (e.g. Dunite, Harzburgite) at the tip of dehydrating faults (Ferrand et al., 2017), and can operate under relatively dry conditions. Catastrophic failure occurs in olivine sub-volumes surrounded by antigorite inclusions (Figure 9). During dehydration stress in antigorite crystals drops to zero and is transferred to the olivine matrix, inducing a mechanical stability. Negative volume changes promote tensile stress concentrations at the tip of dehydrating antigorite clusters, thus facilitating stress transfer (Ferrand et al., 2017). The conditions under which the DDST model can operate are summarized in Figure 10.
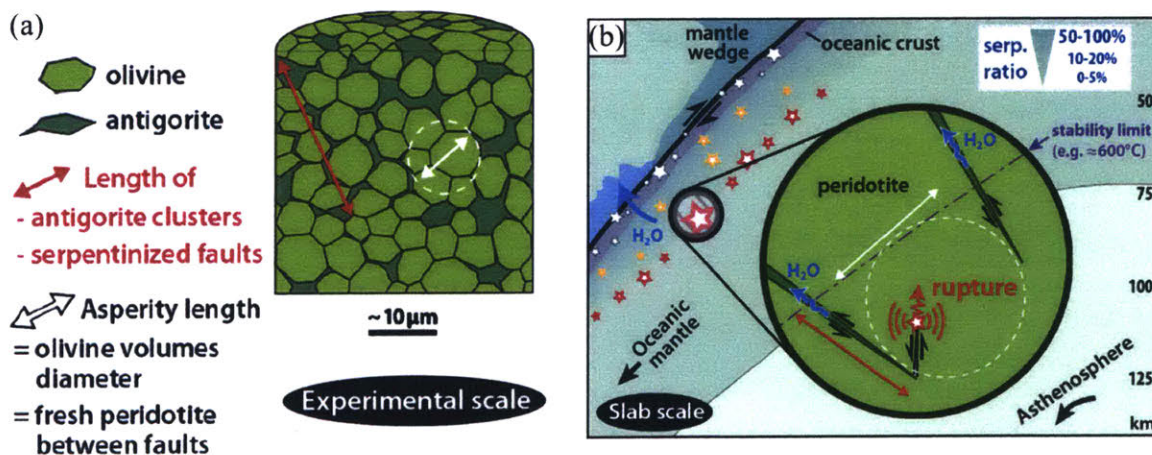
Figure 9. Cartoons with conceptual overview of DDST model. (a) Elementary volume depicting olivine matrix with antigorite inclusions. (b) Conceptual DDST at relevant geological scales. Adapted from Ferrand et al. (2019).

24
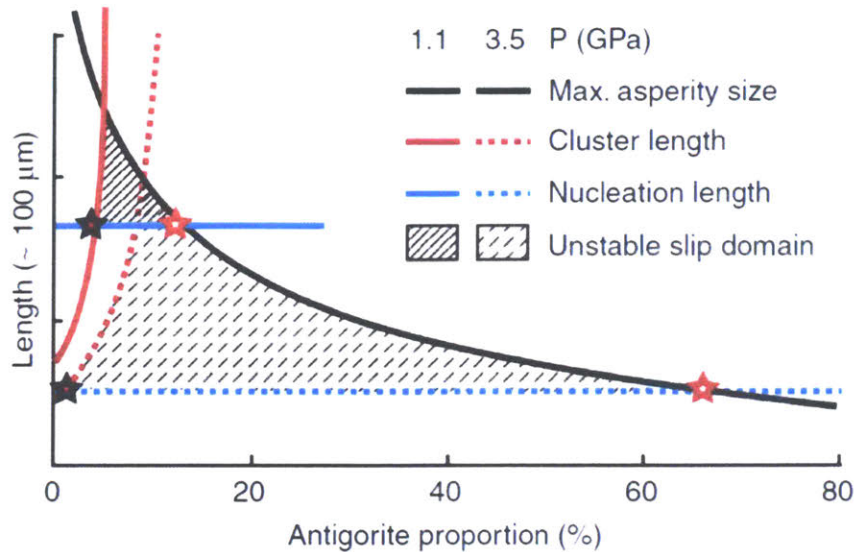
Figure 10. Failure is expected for critical antigorite fractions large enough to transfer a critical amount of stress (black star). Red stars denote a critical nucleation lengths. Adapted from Ferrand et al. (2019).

1.6. Thermal shear runaway instability

Shear localization is produced by a positive feedback between temperature-dependent rheology and shear deformation that generates viscous heating (Griggs and Handin, 1960; Ogawa, 1987; Hobbs and Ord, 1988; Frohlich, 2006; Houston, 2007). The nature of the feedback is such that under certain conditions the localization of shear strain increases and accelerates exponentially, leading to an abrupt failure on a shear zone.

Geological observations support this possibility, evidencing brittle and viscous deformation and the formation of shear zones and pseudotachylite during intermediate-depth earthquakes (John and Schenk, 2006; Mair et al., 2008). Numerical experiments

at least seem in qualitative agreement with these observations (John et al., 2009; Thielmann et al., 2015; Theilmann, 2018). Figure 4 shows field evidence of a shear zone from exhumed mantle rocks, the pseudotachylyte exhibits a molten core and limited deformation at the margins.
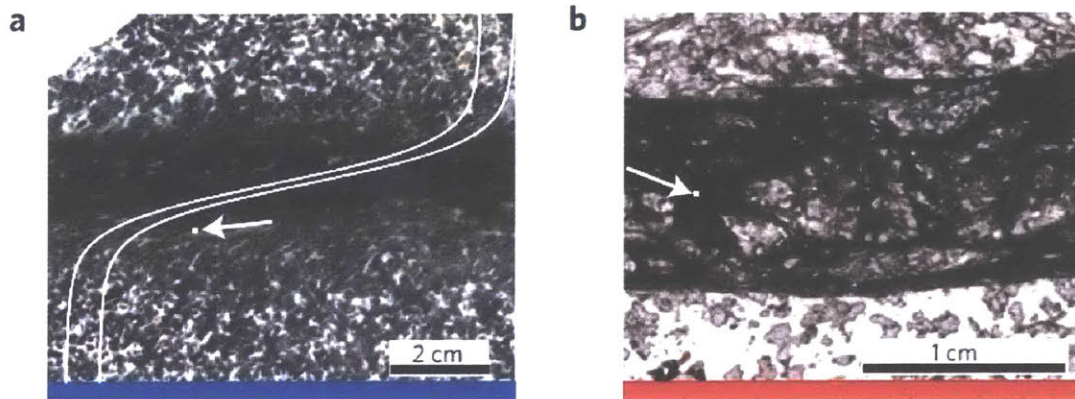
Figure 11. Field observations from a of a typical shear zone and a pseudotachylyte from the Kråkenes gabbro found in a Precambrian terrane in Norway. Adapted from John et al. (2009).

The first seismological observations supporting this mechanism came from a 647 km deep event, the 1994 Mw 8.2 Bolivia earthquake. Kanamori et al., 1998 studied its energy balance. The radiation efficiency, which is the maximum seismic efficiency, was estimated from the radiated energy-to-moment ratio and the static stress drop. A value of about 0.04 was inferred from the data, which is much lower than typical crustal earthquakes (values of 0.1 to 1), a possible mechanism to explain low radiation is that most of the energy released is dissipated in heat rather than in radiating seismic waves.

More recently, Prieto et al. (2013) performed a complete source parameter and energy budget analysis for a population of 253 Mw 3.2–5.2 intermediate-depth

26

earthquakes in the Bucaramanga Nest, Colombia. A combination of high earthquake stress drop and low radiated energy best described the waveforms. Provided a thermal adiabatic model of rapid slip on a finite fault, the temperature may have risen by as much as 600-1000°C, which approaches the melting temperature of (olivine) at these depths (Prieto et al. (2013) and references there in). This again is consistent with substantial shear heating and possibly partial melting.

1.7. Outline of this thesis

In Chapter 2, we develop a novel technique to relocate intermediate-depth events using array processing techniques on teleseismic data. The idea is to be able to automatically pick the seismic phases that best constrain earthquake depth, namely the free-surface P-wave reflections pP and sP. We use two data sets to test our methodology, estimate uncertainties and show the advantages of the method. One of these data sets corresponds to the aftershock sequences of the 2014 Mw7.9 Rat Islands archipelago. The second corresponds to the seismicity along the Chilean subduction zone, a region where a DSZ has been described in previous studies using local networks.

In Chapter 3, we use the methodology developed to study DSZ worldwide. We apply the technique to 32 slab segments and find the DSZ in all of them. This newly developed catalog is then used to study the global characteristics and geometry of DSZ, including the width, depth extent and frequency-size statistics.

Finally, in Chapter 4, we explore the results and suggest possible physical mechanism that explains the seismicity along the DSZ. We suggest that seismicity in the USL and LSL ought to be treated as different types of earthquakes given their difference in magnitude-frequency distributions and in aftershock productivity.

Chapter 2

2. Precise Relative Earthquake Depth Determination Using Array Processing Techniques

2.1. Introduction

In spite of significant advances during the last few decades, the precise determination of an earthquake hypocenter remains one of the outstanding challenges in seismology. Detailed and accurate knowledge of the spatial distribution of seismicity is a key requirement for tectonic processes studies, seismic hazard quantification, earthquake source mechanism analysis and many problems related to Earth structure determination (Engdahl et al., 1998). The dominant source of error when locating earthquakes comes from the lack of detailed knowledge of the three dimensional velocity structure of the Earth (Richards-Dinger and Shearer, 2000), typically a 1-D average velocity model is used and lateral velocity variations arising from 3-D heterogeneities are ignored, resulting in systematic biases in event locations. In many subduction zones these velocity model variations are significant, reaching up to 10% of the reference seismic velocity (Engdahl et al., 1998). To a lesser extent, phase timing errors and the irregular distribution of seismic stations also contribute to hypocenter erroneous locations.

Absolute earthquake location errors can be reduced by jointly inverting for an improved velocity model and a new set of earthquake hypocenters (Magistrale and Sanders, 1996; Pavlis and Booker, 1980; Thurber, 1983). However, recent work has shown the

effectiveness and simplicity of relative relocation techniques (Lin and Shearer, 2005). For nearby events travel time perturbations introduced by unmodeled velocity structure are similar and the application of these techniques significantly reduces relative location errors. In particular, the source-specific station term method (SSST) (Richards-Dinger and Shearer, 2000) and the double-difference algorithm (Waldhauser and Ellsworth, 2000) make it possible to relocate clusters of seismicity distributed over large regional distances.

The SSST is a generalization of the station term method of Frohlich (1979). When seismicity is tightly clustered, static station terms are calculated for each station as the mean of the residuals for all events, a single number at each station accounts for the unmodeled velocity structure. The SSST considers multiple static terms at each station, which are calculated as a function of source position using a Delaunay tessellation (Richards-Dinger and Shearer, 2000). In this way static timing corrections can be consistently applied over large volumes of seismicity.

The double-difference algorithm relies on a similar principle (Waldhauser and Ellsworth, 2000), but it takes a simpler approach, it directly minimizes residual differences for pair of earthquakes without the need to explicitly introduce station corrections. Furthermore, in local and regional studies additional reduction in relative location errors can be archived by using waveform cross correlation to measure differential travel times (Schaff et al., 2002; Schaff et al., 2004; Waldhauser and Ellsworth, 2000). Unfortunately, for earthquakes recorded at teleseismic distances systematically observing a high degree of waveform similarity is challenging. Schaff et al. (2007) attempted to relocate seismicity in global catalogs performing cross correlation for every event pair at every available global

broadband station. For the P arrivals about 12 % of their correlation measurements could be used for relocation. The rate of success for correlating other phases was lower. At teleseismic distances waveform cross correlation may not be as effective.

In routine teleseismic earthquake location, depth is typically the most poorly constrained hypocentral parameter. England et al. (1998) performed a comprehensive absolute relocation of global seismicity and showed that by including depth phases in their relocation scheme depth uncertainties could be significantly reduced, as a result they were able to clearly delineate slab geometry in many subduction zones. Yoshii (1979) used absolute depths, estimated from the travel time difference between the depth phase pP and the direct arrival P (pP-P times) and epicenters reported in ISC catalogs to resolve a DSZ in Northeastern japan, at depths between 80 and 150 km. The separation between the planes of seismicity was 30-35 km, consistent with more recent observations (Brudzinski et al., 2007; Kita et al., 2010). Thus, our ability to interpret many seismotectonic features is limited by the errors in the earthquake locations we plot in cross sections, finding methods to accurately constrain focal depths remains an active area of research.

In this chapter, we focus on the robust determination of relative hypocentral depths. We propose a double difference algorithm that relies on the precise measurement of pP-P differential times using array processing techniques. We start by reviewing the main ideas behind array processing and then progressively develop our relative depth determination scheme. As a first application we analyze a subset of teleseismic records of moderate earthquakes (M 5.5 – M7.0) from a segment of the subducting Nazca plate, beneath northern

Chile. We resolve a DSZ; the two linear patters of seismicity and the seismic gap appear as clear features in our relocations.

This DSZ had been previously characterized by Rietbrock and Waldhauser (2004) using data from a dedicated deployment, with several stations located on top of the segment of interest. Applying our technique, we achieve a similar depth resolution, but using only teleseismic observations. As a second example we relocate the aftershock sequence of the Mw 7.9 Rat Islands archipelago, Alaska, intermediate depth earthquake. The causative plane for this event has been debated in the literature (Twardzik and Ji, 2015; Ye et al., 2014). We provide conclusive evidence in favor of a subvertical rupture plane, consistent with the moment tensor solution for the mainshock. The methods described here are directly applicable to teleseismic relocation of intermediate-depth (50 − 300 km) and deep focus earthquakes (300 - 660 km), however, similar ideas could be used to constrain relative depths of shallower events as well (Ma and Eaton, 2011).

2.2. Double-difference relocation using depth phases

We present double difference algorithm based on double difference that explicitly introduces pP-P time measurements for pairs of events at a given group of stations. We illustrate each step by presenting example measurements from intermediate depth subduction zone earthquakes in Northern Chile.

2.2.1. Depth Phases

Let us consider an earthquake with a depth of 150 km. Figure 12 depicts the ray paths of the P and pP phases. The pP depth phase is a wave that goes straight up from the event and is reflected at the free surface. The time difference pP–P is particularly sensitive to depth (Bondár and Storchak, 2011; Engdahl et al., 1998; Tibuleac, 2014). To illustrate this fact, we perform theoretical calculations of travel times for two events located at depths of 150 km and 140 km, respectively. We use the 1-D reference earth model ak135 (Kennett et al., 1995). For each event the time difference pP-P is plotted as function of event-station distance (Figure 12); there is a consistent gap of about two seconds between the two curves. Depth phases provide the precise constraint on relative earthquake depth.

For large events (M > 6.0) depth phases may be identified by simple visual inspection, however, accurately and systematically picking them is quite challenging, especially when the magnitudes are smaller. Array processing techniques provide a simple, unbiased and consistent way to automatically pick such arrivals (Rost and Thomas, 2002).

33
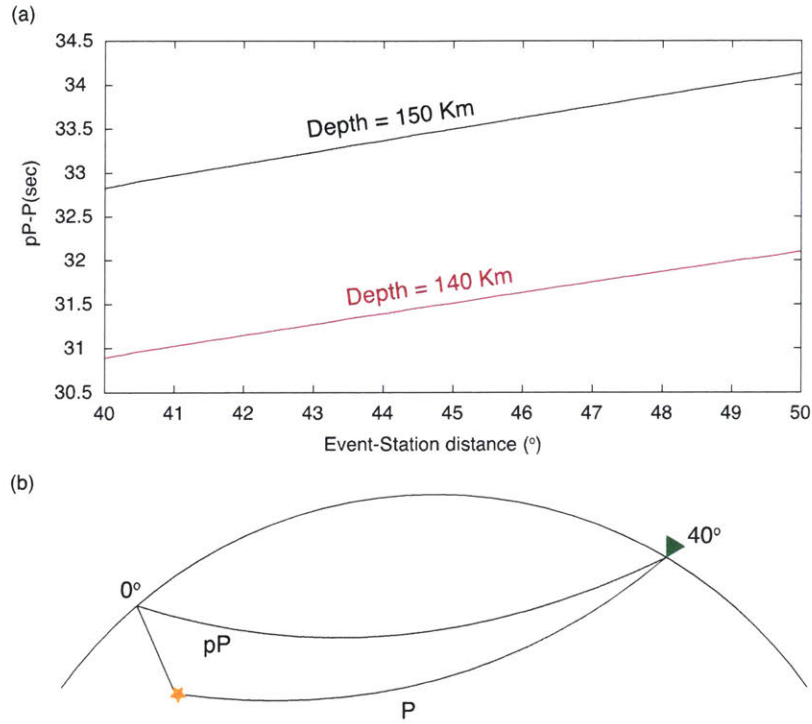
Figure 12. (a) Theoretical pP-P time calculations for two intermediate depth earthquakes using the ak135 Earth model. **(b)** Schematic representation of *P* and *pP* ray paths.

2.2.2. Array based Measurements

Array processing techniques take advantage of the fact that incoherent noise can be suppressed by destructive interference stacking of the signals across all array stations, which also enhances coherent arrivals. For the purpose of our analysis, we will consider arrays as groups of stations where the incident wavefront can be approximated by an incoming plane wave. Two parameters suffice to describe the incoming wave: the back azimuth θ and the horizontal slownesss u_{hor} , beneath the array (Rost and Thomas, 2002). One of the most important applications of array processing in global seismology is the identification of seismic phases, this is done by performing a Vespagram calculation, a diagram that displays

the intensity of the arriving wave as function of slowness and time. Coherent phase arrivals appear as bright spots of concentrated energy in the Vespagram (Rost and Thomas, 2002).

We rely on the vespa process to identify depth phases and to measure pP-P times. First, we estimate the back azimuth of the incoming wave. We use the model ak135 (Kennett et al., 1995) to window the seismograms in the array, we cut 15 second windows around each theoretical P arrival, then we perform a frequency wave-number analysis (f-k analysis) (Rost and Thomas, 2002) to find θ. Once the back azimuth is known multiple beam traces can be calculated (Rost and Thomas, 2002):

$$b_u(t) = \frac{1}{M} \sum_{i=1}^{M} x_i(t - \vec{r}_i \cdot \vec{u}_{hor})$$

Where M is the number of stations in the array, x_i is the displacement seismogram at station x_i, $\vec{r}_i$ is a 2 component vector with the position of the station relative to the center of the array, $\vec{u}_{hor} = u(\sin \theta, \cos \theta)$ is the horizontal slowness vector and $b_u(t)$ is the beam trace for a given horizontal slowness u. This calculation uses the fixed back azimuth θ found by f-k analysis and a suitable range of values for the slowness, between 0.03 and 0.07 sec/km in steps of 0.001 sec/km, for most cases. Before calculating the beam trace each seismogram x_i must be windowed appropriately: a fixed offset from the event origin time must be used, the window must include the theoretical P wave arrival and there should be at least 80 seconds of signal after it, such that the depth phases are present. We cut windows of 160 seconds. To further enhance the coherence of the main phase signals, instead of linearly stacking the

35

signals as in the previous equation, we perform a phase-weighted stack (PWS) with a power of 2 (Schimmel and Paulssen, 1997). Nonlinear stacking techniques provide cleaner Vespagrams and are essential for automating *pP-P* measurements. Figure 13 shows an example of a Vespagram for an M 5.5 subduction zone intermediate-depth earthquake in northern Chile.
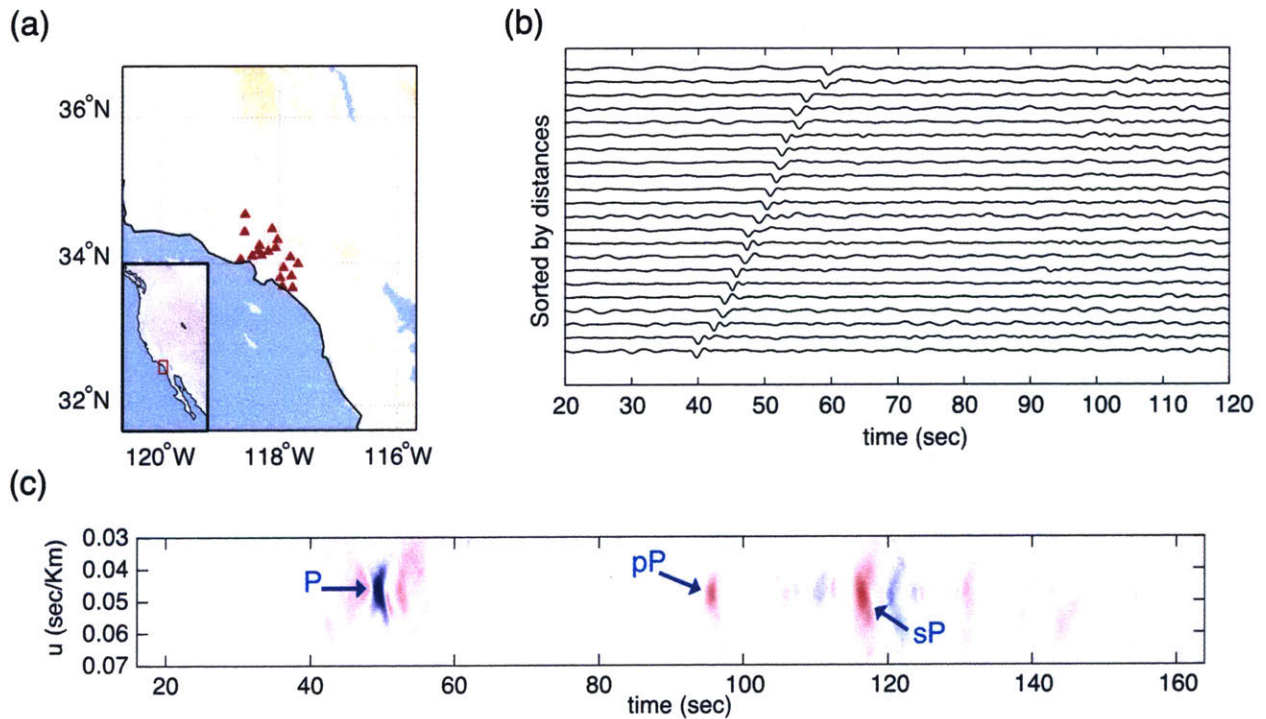
Figure 13. Vespegram analysis for the May 16, 2014, M 5.5, Nazca subduction zone earthquake (latitude=-23.44^o,, longitude =-68.54^o, and depth =105 Km) (a) Map View of a group of broadband seismic stations used as a seismic array, (b) Waveforms from the event band between 0.1 and 1.5 Hz, (c) Computed Vespagram. The *P* arrival and the *pP* and *sP* depth phases appear as clear spots with high energy content. The back azimuth for the incoming wavefront is 138.2^o

At each array we can make one *pP-P* measurement. However, better depth constrains are obtained when a few *pP-P* measurements are available at different distance ranges.

Unfortunately, seismic data is typically collected at regional networks, consisting of stations that spread out over an area that is too wide for array processing techniques to work successfully. To perform the largest possible number of pP-P measurements, we divide regional networks into subarrays, groups of nearby stations where the incident plane wave approximation holds for teleseismic arrivals (Rost and Thomas, 2002). To select the subarrays, we take the area spanned by the stations of interest and overlay a grid, in such a way that a large number of grid cells will contain a significant number of stations. We only build subarrays at grid cells where the number of stations is at least 10. Note that over time regional networks may add or remove stations, but the grid must remain fixed, such that consistent measurements can be made for events that happen at widely different times. At different periods a subarray may gain or lose a station, but its center will remain roughly constant. In Figure 14. we show an example of the subarrays used to relocate seismicity in a segment of the Nazca Subducting plate (see section 3.1). Stations of networks AZ, BK, CC, CI, MB, NC, NN, SN, UO, UU, UW, US and WY, that span the western United States, are included. All grid cells have the same size, 2.2°x2.2°. In total 12 subarrays were used to perform the measurements.
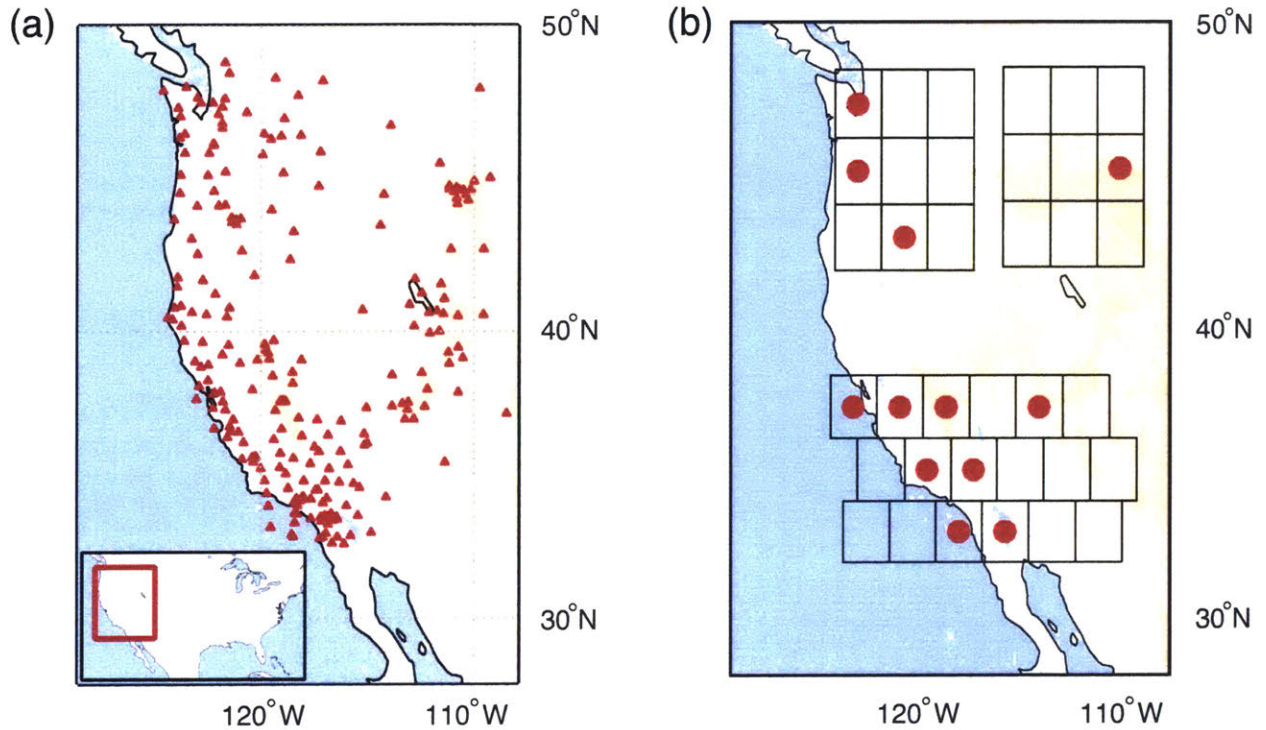
Figure 14. (a) Distribution of broadband permanent stations for regional network: AZ, BK, CC, CI, MB, NC, NN, SN, UO, UU, UW, US, and WY. **(b)** Grid used to construct subarrays, red dots indicate grid cells with 10 or more stations, these are the subarrays where pP-P can be measured.

2.2.3. Relative earthquake depth determination algorithm

Let us assume that we have multiple events, clustered in space, and a set of subarrays where measurements are performed. For a given event observed at a particular subarray we first estimate its back azimuth and with it we compute the Vespagram for the incoming wavefront (Rost and Thomas, 2002). Incoherent noise is removed by applying phase-weighted stacking techniques (Schimmel and Paulssen, 1997). We only make a measurement if the SNR around the stacked P wave is larger than 5. The pP depth phase is the second arrival and normally it is the clearest depth phase, provided we use vertical component

seismograms and the focal mechanism of the event is favorable. Since the Vespagram is calculated in the time domain we can directly measure the *pP-P* time from it. The polarity of the phases can also be read directly from the Vespagrams. In Figure 15, for example, the polarity of the *pP* phase is flipped with respect to that of the *P* wave. We automate the process, for each subarray we measure the *pP-P* time by looking for the first two absolute maxima in the Vespagram. This kind of simple automation is only possible when phase-weighted staking is used to enhance the main arrivals, when linear stacking is performed the excess noise can make automatic measurements unstable and unreliable.

Let us now consider event pair (i, j) observed at subarray k, if the two events are close together, we may formally define the observed differential time as:

$$\Delta t_{i,j,k}^{obs} = (pP - P)_i - (pP - P)_j$$

As an example, the Vespagrams for two subduction zone earthquakes in the Nazca plate (M 5.8 and M 6.0) are shown in Figure 18. The two events are close to one another, with a depth separation of about 13 km, and yet, a simple visual inspection reveals that Δt^{obs} must be significant.
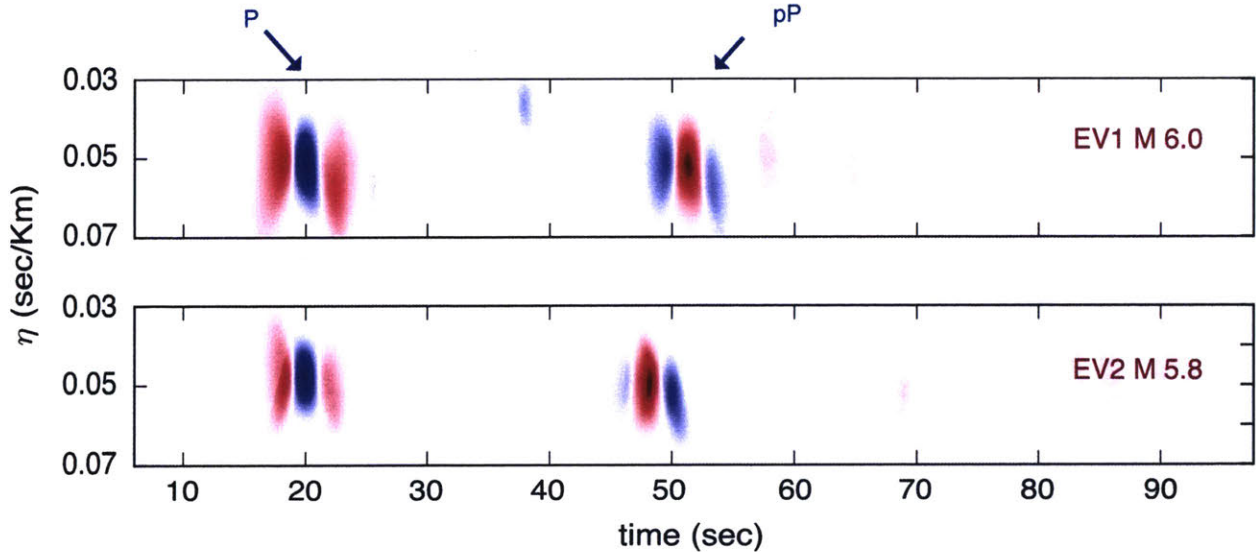
Figure 15. Vespagram analysis for the May 16, 2014, M 5.5, Nazca subduction zone earthquake (latitude=-23.44^o, longitude =-68.54^o, and depth =105 Km), (a) map view of the array of broadband seismic stations, (b) waveforms from the event band between 0.1 and 1.5 Hz, (c) computed Vespagram. The P arrival and the pP and sP depth phases appear as clear spots with high energy content. The back azimuth for the incoming wavefront is 138.2^o.

Subarray level measurements share some similarities with those performed at a single station. By taking the center of the subarray as a reference point we compute the event-subarray distance over the surface of the spherical earth. Then, we measure the *pP-P* time for each subarray and plot the results as a function of event-subarray distance. As an example, Figure 16 shows our measurements at the 12 subarrays constructed using stations from regional networks in the Western United States (Figure 14). Another pair of subduction zone earthquake in the Nazca plate (M 5.6 and M 5.5) is used. We fit our data using the ak135 1-D reference earth model (Kennett et al., 1995). The estimated depths are also shown. Note that most of the deviations from the model are consistent for both events, resembling path specific terms (Richards-Dinger and Shearer, 2000), which would cancel out when the double difference is computed.
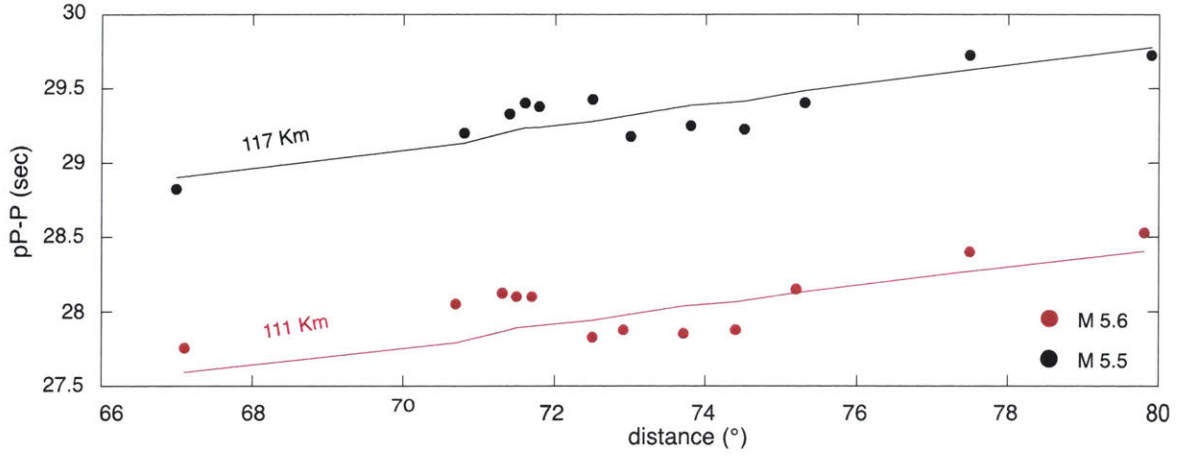
Figure 16. Measurements for two earthquakes at the 12 subarrays shown in Figure 17, the best fitting model depths are also displayed. The M 5.6 event ruptured in November 10, 2014 (latitude $=-21.63°$, longitude $=-68.72°$)) and the M 5.5 earthquake happened in December 4, 2008 (latitude $=-21.35°$, longitude $=-68.25°$). Both events occurred in the Northern segment of the Nazca plate.

Once Δt^{obs} is measured for every event pair at every available subarray, we invert for the best fitting relative depths using a procedure similar to Waldhauser and Ellsworth (2000). The 1-D reference Earth model ak135 (Kennett et al., 1995) is used for theoretical travel time calculations. The best fitting depths are found by minimizing the residual between observed and predicted differential times:

$$r = \sum_{i,j,k} \left(\Delta t_{i,j,k}^{obs} - \Delta t_{i,j,k}^{cal}\right)^2$$

where $\Delta t_{i,j,k}^{cal}$ is the predicted differential time,

$$\Delta t_{i,j,k}^{cal} = (pP - P)_i^{cal} - (pP - P)_j^{cal}$$

41

Calculated for event pair i, j at subarray k. $\Delta t_{i,j,k}^{obs}$ is the observed differential time directly measured from the Vespagrams as previously discussed. $pP\text{-}P$ measurements are mostly sensitive to earthquake depth; therefore, we do not attempt to solve for the event epicenters, we keep the latitudes and longitudes provided in the catalog and use an iterative nonlinear conjugate gradient algorithm to find the set of hypocentral depths that minimizes the residual r (Aster et al., 2005; Shewchuk, 1994).

2.3. Applications

We explore two possible applications of the technique. The first one serves as a validation; it reexamines the structure of a known DSZ in the Nazca subducting plate. In the second one the aftershock sequence of the 2014 Mw 7.9 Rat Islands archipelago intermediate depth earthquake is analyzed in an attempt to illustrate the key role played by accurate relative depth determination when constraining structures at depth.

2.3.1. Double seismic zone in the Nazca subducting plate

The spatial distribution of seismicity provides important information about the physical processes that happen within the subducting lithosphere. It has been repeatedly shown that DSZ are a dominant pattern of seismicity in many, if not all, subduction zones (Brudzinski et al., 2007; Cassidy and Waldhauser, 2003; Hacker et al., 2003; Rietbrock and Waldhauser, 2004). In particular, double-difference relocation on data collected by the ANCORP dedicated local deployment (Oncken et al., 1999) was used to map the detailed structure of clustered seismicity around a segment of the Nazca subducting slab in Northern Chile. A DSZ with a gap of 10 km was observed (Rietbrock and Waldhauser, 2004).

We test our relocation scheme on the very same segment of the Nazca Plate as studied by Rietbrock and Waldhauser (2004). Initial hypocenter locations are extracted from the NEIC global earthquake bulletin (PDE catalog) for the period 2005-2016. We use stations that are 30° to 90° away from the event cluster, this avoids mantle triplications that contaminate P and pP arrivals. To build subarrays we also need a sufficiently dense network that has been operational for the period of interest. Thus, we focus our attention on the Western United States, the regional networks: AZ, BK, CC, CI, MB, NC, NN, SN, UO, UU, UW, US and WY, when combined, are reasonably dense and all of them started their operation before the year 2005. We construct 12 subarrays as shown in Figure 14 and discussed in section 2.2. For each event we only perform a measurement at a given subarray if the signal to noise ratio around the stacked P wave is larger than 5. To include an event in our relocation scheme we require at least 3 pP-P measurements at different subarrays. Our SNR criteria was only met by events with M > 5.5. For the period of interest 32 such events were found in the catalog, of those we were able to relocate 30. The selected events and the area of interest are shown in Figure 17, earthquakes with M>3.0 are also displayed, we plot the same cross section as in Rietbrock and Waldhauser (2004).
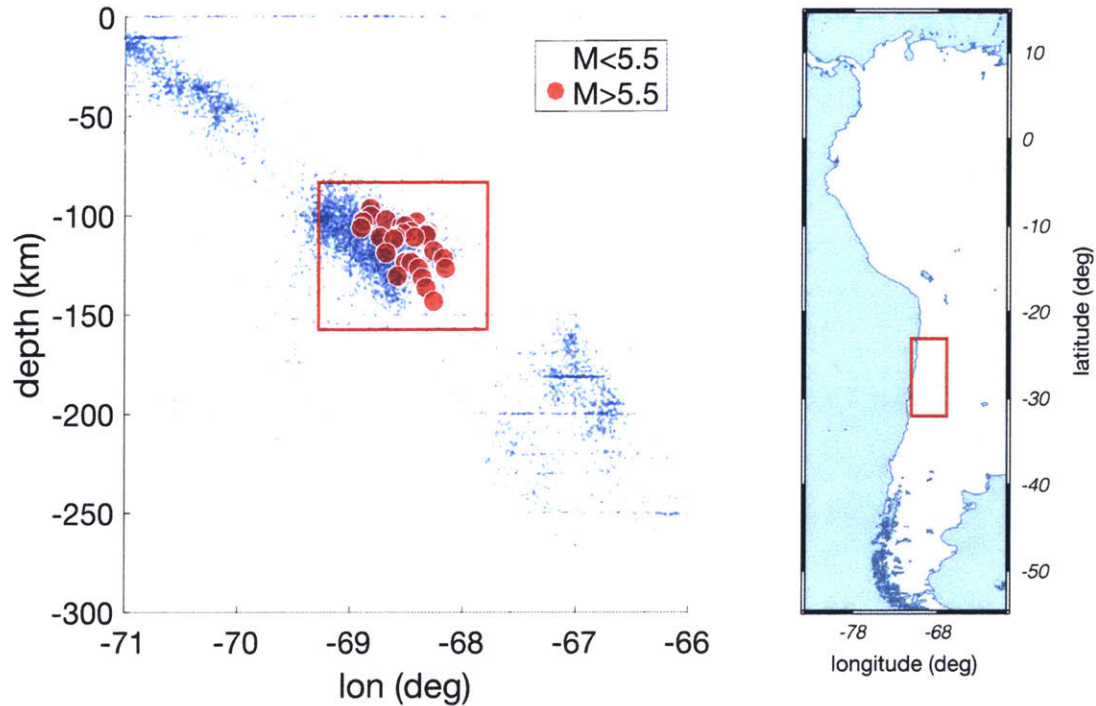
Figure 17. W-E cross section of the Nazca subducting plate segment under study. M <5.5 PDE catalog events for the period 2005-2016 are shown in blue. The events with M>5.5 used in this study are shown in red.

Once all possible *pP-P* measurements are made, we invert for the best fitting relative depths using the procedure described in section 2.3. Figure 18 shows the results of our inversion and the comparison with the initial catalog locations, the two linear patterns of seismicity are clearly resolved, the seismic gap between them is also evident. We measure the width of the DSZ using a technique similar to the one proposed by Brudzinski et al. (2007). First, we determine the average dipping direction of the slab. Then, we compute a histogram using the distances of the events along the slab-normal direction. Finally, we fit a bimodal Gaussian distribution to the histogram (Figure 18). The width of the DSZ is given by the distance between the two peaks of the distribution. We obtain a width of 13.2 $\pm$ 1.8 km. The error is estimated using the 95% confidence interval of the bimodal fit.
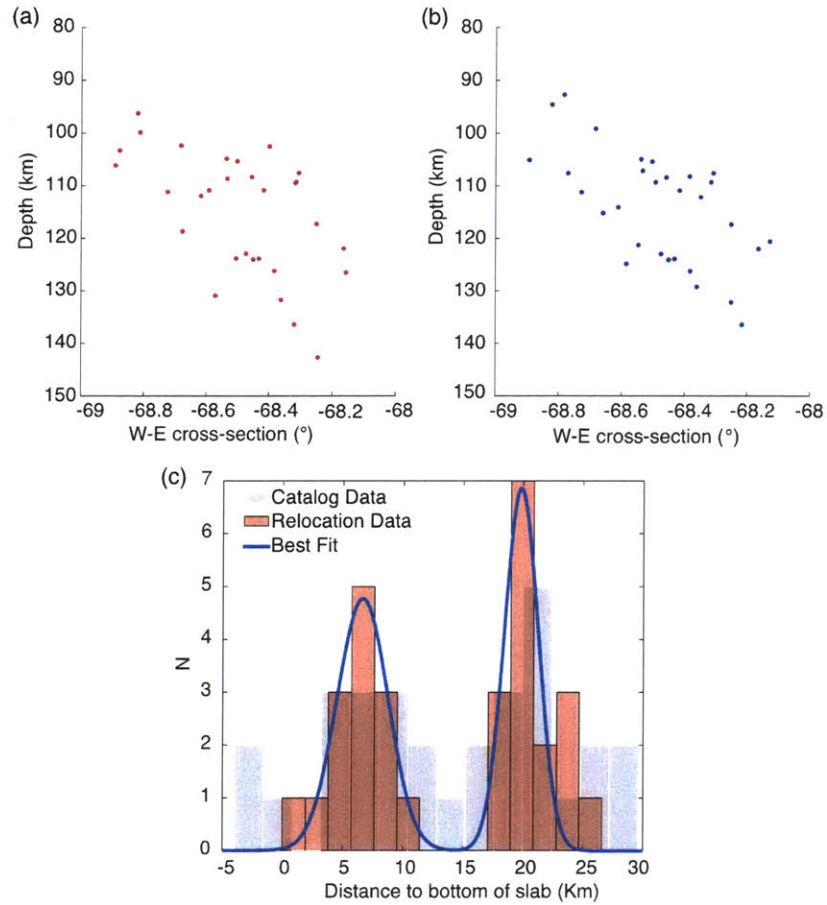
Figure 18. DSZ in the northern segment of the Nazca plate. (a) Initial PDE catalog hypocenters, (b) event relocations with improved relative depths, (c) histogram perpendicular to slab down-dip direction and bimodal gaussian fit.

2.3.2. The Mw 7.9 Rat Islands archipelago, Alaska, intermediate depth earthquake

On June 23, 2014 one of the largest intermediate depth earthquakes to date ruptured beneath the Rat Islands archipelago in the Western Aleutians Islands, Alaska (Ye et al., 2014). This Mw 7.9 event happened within the subducting pacific slab in a region of oblique plate motion, where the pacific plate is moving relative to the North American plate at a rate

of about 75 mm/yr (DeMets et al., 1990). The global centroid moment tensor (GCMT) solution is well approximated by a double-couple point source model, with two nodal planes: a steeply-dipping plane with strike 309°, dip 84° and rake -117° and a shallow-dipping plane with strike 207°, dip 27° and rake -13°. Ye et al. (2014) performed a detailed source analysis, favoring the shallow-dipping plane. However, Twardzik and Ji (2015), based on relocated aftershocks, argue in favor of a steeply dipping causative fault plane.

At least 28 aftershocks (Mw > 4.5) with depths spanning 90 to 150 km were generated, most of them could be observed at teleseismic distances. This is an example of highly clustered seismicity at depth, where earthquake relocation methods would allow for precise relative hypocentral depth determination. For this analysis, we use data form the Japanese High Sensitivity Seismograph Network (Hi-Net). Most Hi-Net stations are between 34° and 38° from the events of interest. This is the closest distance range for which clean pP arrivals could be observed. The Western United States is further away, 60° to 70°, and the Alaska local network is too close, 20° to 25°. Hi-Net offers a dense network with the best possible signal to noise ratio for pP arrivals. As in the previous example we use a grid to build subarrays. We select 12 subarrays where pP-P measurements can be performed, each subarray contains between 15 and 21 stations (Figure 19). In this case grid cells are 2°x2°. Again, we only accept pP-P measurements if the SNR around the stacked P wave is larger than 5. Also, to include an earthquake in our relocation scheme we require at least 3 pP-P measurements at different subarrays. We were able to relocate a subset of 17 Mw > 4.9 aftershocks. In Figure 19 we plot our measurements as a function of event-subarray distance for a few representative events. The vertical axis is flipped because pP-P is an excellent proxy

46

for depth. A picture of the relative distribution of seismicity already emerges; there is a consistent travel-time gap of about 2 seconds, which would translate into a gap at depth.
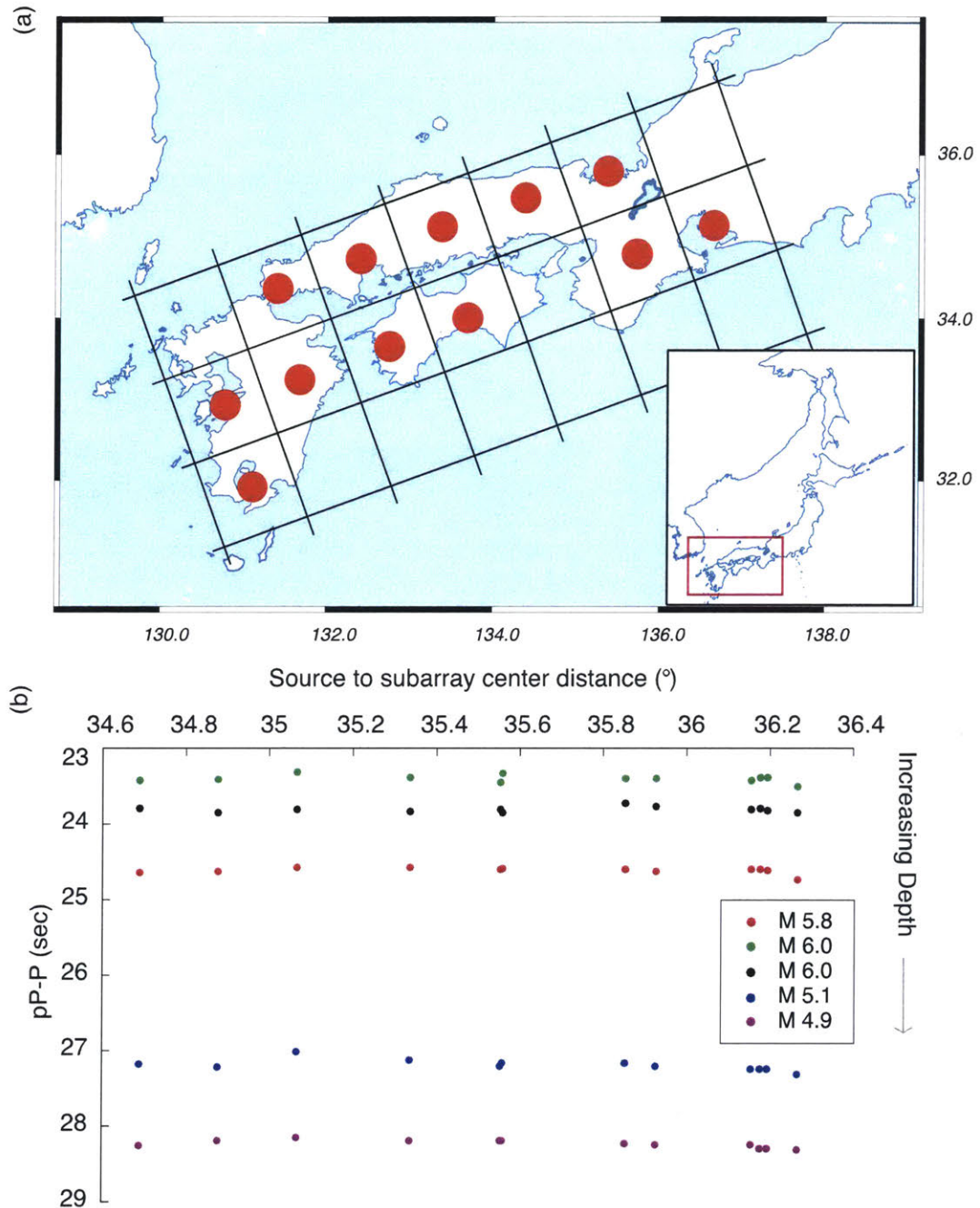
Figure 19. (a) Grid with 12 subarrays where measurements were performed. Each grid cell contains between 15 and 21 Hi-Net stations. The inset displays a map view of Japan (b) pP-P measurements as a function of event-subarray distance for 5 representative aftershocks. Vertical axis is flipped.

47

In Figure 20 we compare catalog locations with our best fitting relocations. Note that improved depths lead to sharper distribution. The offsets between the catalog depths and the new relative depths range from 1.5 km to 14.4 km, with a mean of 5.2 km. Cross section A-A' runs perpendicular to the steeply dipping nodal plane, whose projection is denoted by the thick red line. Similarly, cross section B-B' runs perpendicular to the shallow-dipping nodal plane, whose projection is also denoted by a thick red line. The relocated aftershocks align quite well along the steeply dipping nodal plane. In cross section B-B' a dashed line with an inclination of 63° is shown, this corresponds to the projection of the steeply-dipping nodal plane. Figure 20e shows a clear alignment of the relocated aftershocks with the steep plane. Our results are not consistent with a shallow-dipping nodal plane. Therefore, we can confidently assign the causative fault plane to the steeply dipping one, in agreement with Twardzik and Ji (2015).
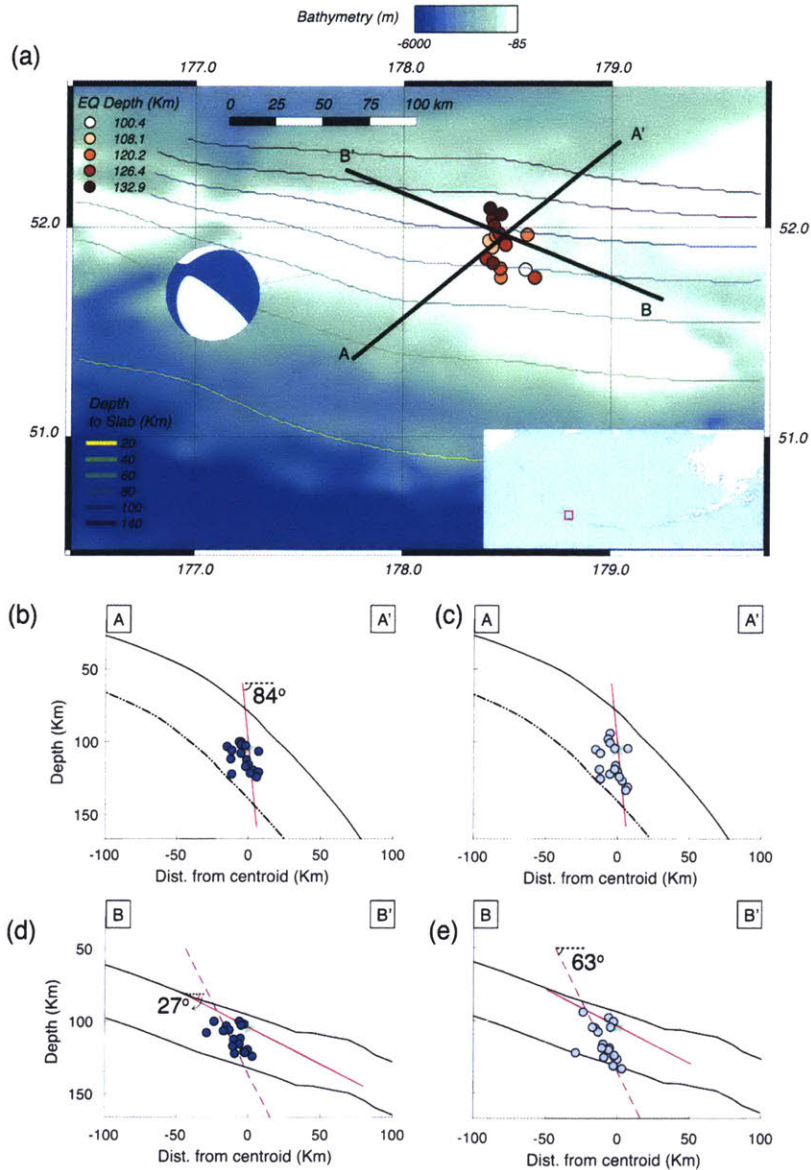
Figure 20. (next page). (a) Map view of the area of interest, contour lines follow the USGS slab1.0 model and are color coded by their depth to the top of the slab, the set of 17 relocated aftershocks is shown and is color coded using catalog depths, the two thick black lines represent the cuts for profiles A-A' and B-B'. The moment tensor solution for the mainshock is also shown **(b)** Cross section perpendicular to the steeply dipping nodal plane, the red line is the projection of the corresponding steeply dipping plane, catalog locations are shown. **(c)** Same cross section as in panel (b), however the set of events is plotted using our best fitting relative depths. **(d)** Cross section perpendicular to the shallow-dipping nodal plane, the red line is the projection of the corresponding shallow-dipping plane, the black dashed line is the projection of the steeply dipping nodal plane, catalog locations are shown. **(e)** Same cross

49

section as in panel (d), however the set of events is plotted using our best fitting relative depths.

2.4. Limitations and potential applications

The methodology described here can be applied to records of earthquakes that meet the following criteria:

- The events are large enough to be observed by a seismic array or a number of subarrays. At teleseismic distances the lowest detectable magnitude is around 5.0, although this depends on the quality of the stations and the event-subarray distance. New stacking techniques (e.g., Korenaga, 2013) may allow for the location of smaller earthquakes.

- Depth phases are present, have good signal-to-noise ratio and are separated in time from other phases (e.g., P, S, sP, PcP). In our examples, we used the pP phase for intermediate depth earthquakes (50-300 km), therefore, source-subarray distances range between 30° and 90°.

- The method can directly be applied to deep focus earthquakes (depth > 300 km). For such events clear depth phases are available in the main shock as well as in many aftershocks (Zhang et al., 2014). In this scenario a distance range of 30° to 90° is also appropriate, although care must be taken to avoid ranges where PcP arrivals interfere with the pP phase.

- Depth phases at regional distances can also be used. For example, the *sP* phase is observed between 8° to 15°. In principle, smaller distance ranges result in higher signal to noise ratios, this may allow for the location of a large number of smaller events, however this kind of application is beyond the scope of this work.

- Other authors (Ma and Eaton, 2011) have suggested using depth phases associated with shallow interphase reflections to improve depth constrains for shallower events (depth < 20 km). If arrays are available, our method could be helpful.

- Shallow earthquakes (depth < 50 km) observed at teleseismic distances have depth phases arriving close in time to the main *P* arrival (Warren and Shearer, 2005; Denolle and Shearer, 2016; Houston and Kanamori, 1986). Depending on the source duration the *pP* or the *sP* phase could interfere with the *P* wave. Our technique would require additional modifications, such as source deconvolution, to be useful in such situations.

2.5. Error Analysis

2.5.1. Phase Timing Error

We now assess the quality of the relative depth estimates. Subarrays tend to be heterogeneous, with a varying number of stations, uneven spatial coverage and different geographical extents. Error quantification must be done in such a way that it reflects the impact of these considerations.

Let N be the total number of subarrays and let k_i be the number of stations at subarray i. To capture the variability of the possible geometric configurations, we use a bootstrap resampling scheme. We conduct $R = 4000$ experiments. When experiment r is performed, we invert for $\mathbf{z}_r^*$, the resulting set relative depths, as follows:

1. For each subarray i we remove 2 stations at random, this results in N new subarrays, each with $k_i - 2$ stations.

2. We compute Vespagrams for all available event pairs at all the newly defined subarrays, perform measurements of pP-P times, and invert for the best fitting relative depths $\mathbf{z}_r^*$.

The bootstrap variance is given by (Davison and Hinkley, 1997):

$$var[\mathbf{z}^*] = \frac{1}{R-1} \sum_{r=1}^{R} (\mathbf{z}_r^* - \bar{\mathbf{z}}^*)^2$$

where

$$\bar{\mathbf{z}}^* = \frac{1}{R} \sum_{r=1}^{R} \mathbf{z}_r^*$$

Is the average over all R experiments. We use $2\sqrt{var[\mathbf{z}^*]}$ as a conservative estimate for the error. For the Double Seismic Zone in the Northern segment of the Nazca plate (section 2.4.1), we obtain and average relative depth error of 1.8 km, error bars for all of the events are shown in Figure 14. For the aftershock sequence of the Mw 7.9 Alaska, intermediate depth earthquake (see section 2.4.2. for details), we obtain an average depth error of 1.9 km (Figure 21).
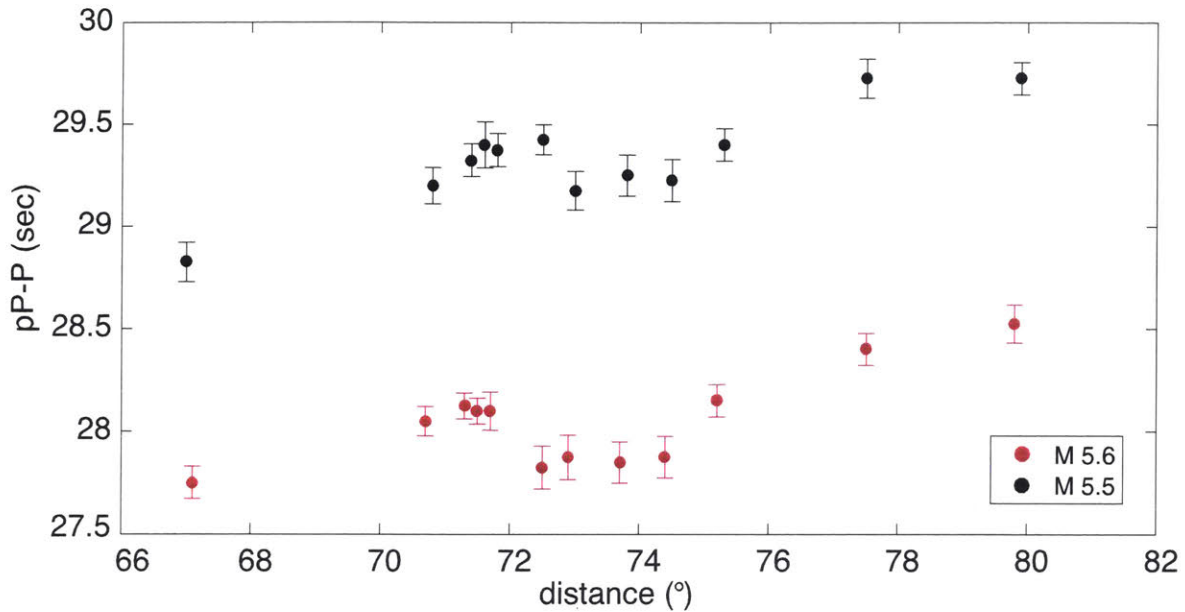
52

Figure 21. Error bars for measurements of the pP-P times at the 12 subarrays shown in Figure 14. The M 5.6 event, in red, ruptured in November 10, 2014 (latitude = -21.63^o, longitude = -68.72^o). The M 5.5 earthquake, in black, happened in December 4, 2008 (latitude = -21.35^o, longitude = -68.25^o). Both events were included in the relocation example discussed in section 3.1.

We now make a crude estimate of the order of magnitude of the error expected after relocation. Assuming that the *pP* takes off straight up into the earth's surface and that the *P* wave velocity at the source is 8 km/sec, a depth error of about 1.1 km would be expected. This is of course a crude calculation but it provides an insight into the resolution of our relocation scheme.

2.5.2. Relative Depth Errors

We now assess the quality of the resulting relative depths. Given the limited station availability subarrays tend to be heterogeneous, with a varying number of stations, uneven

spatial coverage and different geographical extents. Error quantification must be done in such a way that it reflects the impact of these considerations.

Let N be the total number of subarrays and let k_i be the number of stations at subarray i. To capture the variability of the many possible geometric configurations, we use a bootstrap resampling scheme. We conduct $R = 4000$ experiments. When experiment r is performed, we invert for $\boldsymbol{z}_r^*$, the resulting set relative depths, as follows:

3. For each subarray i we remove 2 stations at random, this results in N new subarrays, each with $k_i - 2$ stations.

4. We compute Vespagrams for all available event pairs at all the newly defined subarrays, perform measurements of pP-P times, and invert for the best fitting relative depths $\boldsymbol{z}_r^*$.

The bootstrap variance is given by (Davison and Hinkley, 1997):

$$var[\boldsymbol{z}^*] = \frac{1}{R-1} \sum_{r=1}^{R} (\boldsymbol{z}_r^* - \bar{\boldsymbol{z}}^*)^2$$

where

$$\bar{\boldsymbol{z}}^* = \frac{1}{R} \sum_{r=1}^{R} \boldsymbol{z}_r^*$$

Is the average over all experiments. We use $2\sqrt{var[z^*]}$ as a conservative estimate for the error. For the Double Seismic Zone in the Northern segment of the Nazca plate (section 3.1), we obtain and average relative depth error of 1.8 km, error bars for all events are shown in Figure 22. For the aftershock sequence of the Mw 7.9 Alaska, intermediate depth earthquake (see section 3.2 for details), we obtain an average depth error of 1.9 km (Figure 23).
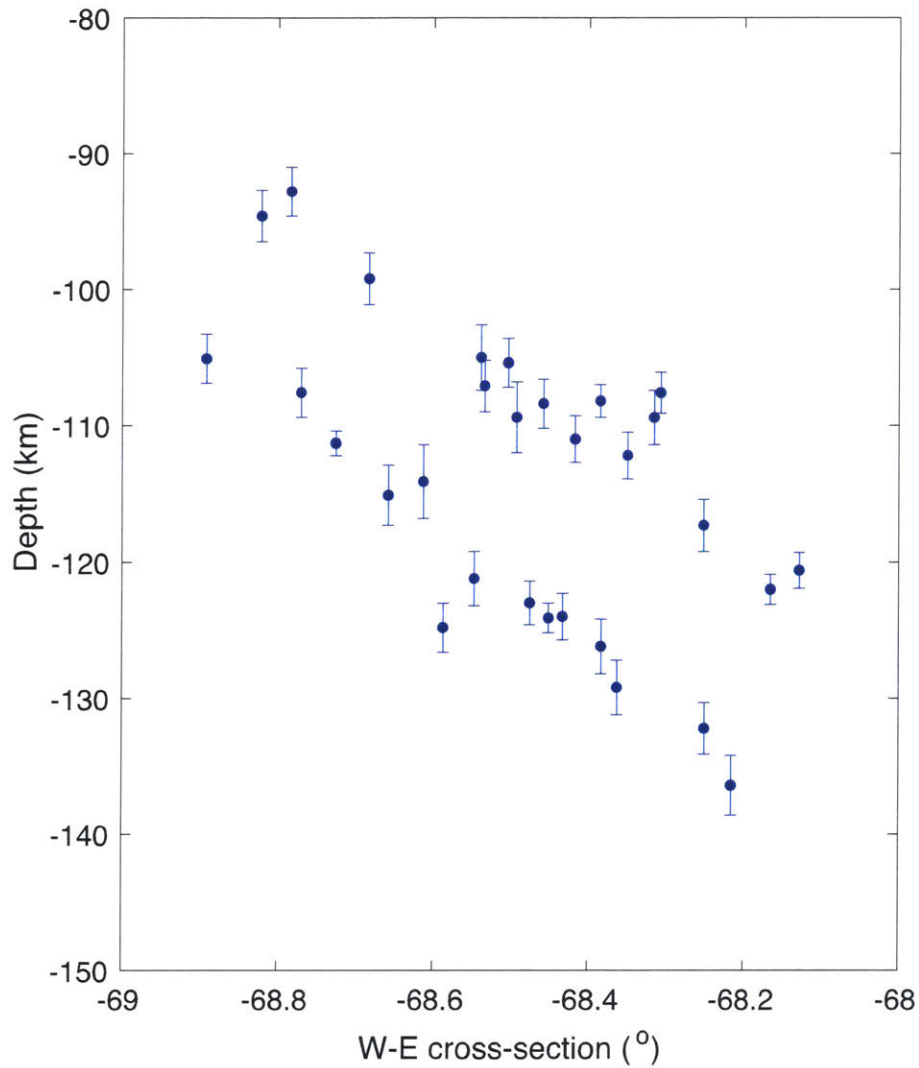
Figure 22. Error bars for all events in the Double Seismic Zone of the Northern segment of the Nazca plate.
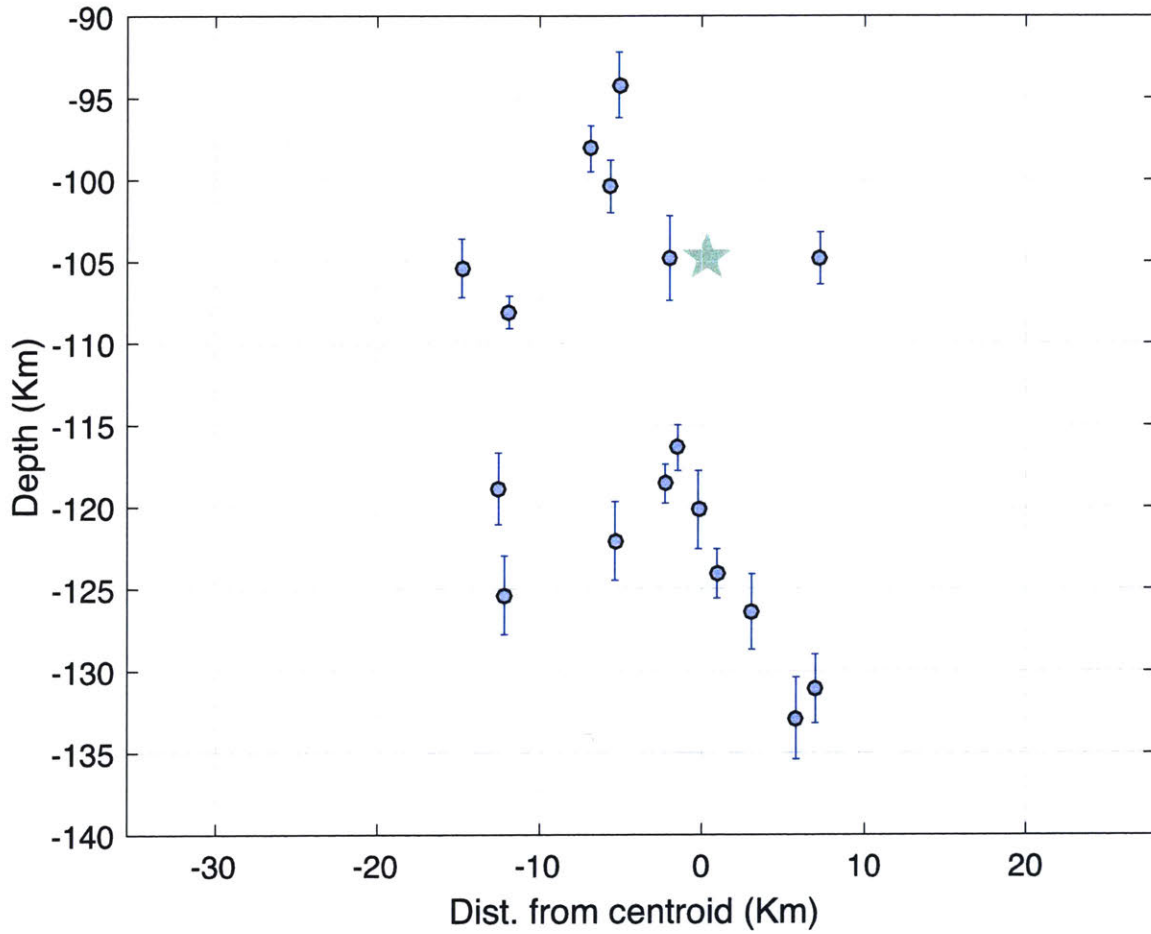
Figure 23. Error bars for a set of 17 aftershocks of the M 7.9 Rat Islands archipelago, intermediate depth earthquake. A cross section perpendicular to the steeply dipping nodal plane is plotted, A-A' in Figure 20. The star corresponds to the GCMT centroid of the main shock.

Chapter 3

3. Controlling Factors of Seismicity and Geometry in Double Seismic Zones

3.1. Introduction

Double Seismic Zones (DSZ) are a common feature of seismicity in subducting

slabs (Brudzinski et al., 2007). Multiple studies have shown that earthquakes within the

subducting lithosphere cluster into two distinct layers (Hasegawa & Nakajima, 2017;

Hasegawa et al., 1978; McGuire & Wiens, 1995; Rietbrock & Waldhauser, 2004) that

eventually merge at depth (Green et al., 2010; Wei et al., 2017). The region between the

two has little or no seismicity and their average separation correlates with plate age

(Brudzinski et al., 2007). Earthquakes located in the upper seismicity layer (USL) are

inferred to occur within the subducting oceanic crust and/or uppermost mantle, while the

lower seismicity layer (LSL) appears to occur in the subducting lithospheric mantle (Green

et al., 2010; Peacock, 2001; Wei et al., 2017). Seismicity in the USL is generally believed

to be due to fluid overpressure linked to dehydration reactions within the crust or

uppermost mantle (Hacker et al., 2003; Kirby, 1995; Houston 2015, Okazaki & Hirth,

2016). In contrast, the mechanism for seismicity in the LSL is much more controversial

(Ohuchi et al., 2017; Peacock, 2001; Reynard et al., 2010, Ferrand et al., 2017). Recent

work in the laboratory and field observations suggest that faulting at intermediate-depths

may occur under dry conditions (Ouchi et al., 2017; Scambulleri et al., 2017), although it

was recently shown that a partially hydrated lithospheric mantle could produce failure by a

stress transfer mechanism driven by dehydration reactions in a partially hydrated uppermost mantle (Ferrand, 2017; Scambulleri, 2017; Kita and Ferrand, 2018).

A possible pathway for water to infiltrate into the subducting mantle is through faulting and plate bending at the trench (Faccenda et al., 2009; Faccenda et al., 2012; Korenaga, 2017; Ranero et al., 2003), although how deep can water go and how pervasive this mechanism could be, remain controversial (Korenaga, 2017; Syracuse et al., 2008). Reduced Vp anomalies are often found along the LSL (Dorbath et al., 2008); in some cases, the high Vp/Vs ratios expected for a highly serpentinized mantle or fluid saturated rock are not observed (Dorbath et al., 2008; Syracuse et al., 2008), while other results point towards a hydrated lithospheric mantle (Cai et al, 2018; Bloch et al., 2018). Anisotropy of anhydrous peridotite may provide a better explanation for the inferred seismic velocity anomalies (Hasegawa & Nakajima, 2017; Ranero et al., 2003), imposing an additional constraint on the triggering mechanism: it must also operate under relatively dry conditions. Therefore, brittle-like failure driven by a thermal shear instability is also viable and potentially more likely (Ohuchi et al., 2017; Kelemen & Hirth, 2007, John et al., 2009) for earthquakes in the LSL.

The presence (or absence) of fluids (among other factors) is known to affect the relative number of small to large earthquakes in subduction zones (Katsumata, 2006; Wiemer & Benoit, 1996; Wyss et al., 2001, Kita and Ferrand, 2018), i.e., the b-value in the frequency-size distribution of seismicity; a small b-value implies a relatively large number of big events. In Alaska, New Zealand, Japan, and the Lesser Antilles high b-value anomalies take the shape of a bull's-eye, at the top of the slab, and correlate with regions where dehydration reactions are expected (Katsumata, 2006; Wiemer & Benoit, 1996).

Additionally, b-value measurements have become proxies for the presence of fluids under volcanic arcs (van Stiphout et al., 2009; Wyss et al., 2001). Accurate locations combined with careful statistical analysis offer the unique opportunity of assessing the relative abundance of fluids and the triggering mechanism of earthquakes in DSZ worldwide.

We systematically apply the relocation method proposed by Florez and Prieto (2017) to generate a new global catalog of intermediate-depth seismicity. This dataset enables us to study 32 slab segments that sample a broad range of subducting slab physical conditions, including plate ages, convergence velocities, and thermal parameter (e.g., Wiens, 2001), determined from the slab's age, convergence velocity and dip angle (Figure 24). We investigate the relationship between width and depth-extent of DSZs and the physical properties of the subducting slab; and analyze the statistical behavior of seismicity in the USL and the LSL in terms of both productivity and frequency-size distribution.
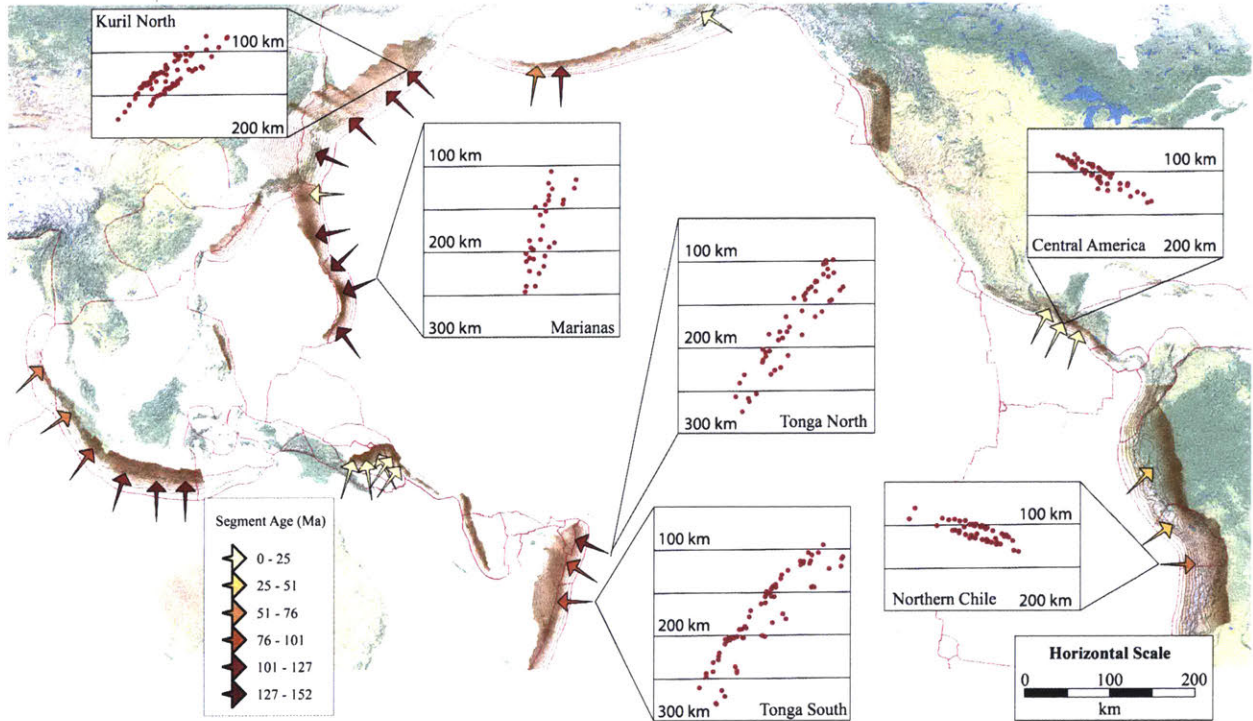
Figure 24. Global map view of major subduction zones with depth contours (orange lines) that follow the Slab1.0 model (Hayes et al., 2012). Arrows represent the segments analyzed, point in the direction of relative plate motion and are color-coded by age. Vertical cross-sections display the improved locations (red dots) and are drawn at the same scale. At each segment analyzed a DSZ was observed, making this pattern of seismicity a global feature as first proposed by Brudzinski et al. (2007).

3.2. Earthquake Relocation using Depth-Phases

The width of a DSZ varies from a few to about 40 km (Brudzinski et al., 2007). When compared with this length scale typical location errors in global seismicity catalogs can be significant. Hypocentral depth is particularly problematic most event locations in global catalogs have well constrained epicenter, due to good azimuthal coverage, but lack vertical resolution (Engdahl et al., 1998). The main sources of error affecting the accuracy of global seismicity catalogs are: i) random phase picking errors (Richards-Dinger & Shearer, 2000; Shearer, 1997), ii) systematic biases introduced by using an average 1-D velocity model

(Lin & Shearer, 2005; Waldhauser & Ellsworth, 2000), which is especially important in subduction zones where lateral velocity variations can be as large as 10% of the background model (Engdahl et al., 1998), and iii) insufficient use of phases whose ray-paths have good vertical coverage (Engdahl et al., 1998). Depth errors of about 40 km are not uncommon (Engdahl et al., 1998).

To overcome these limitations, we use the algorithm developed by Florez and Prieto (2017), first applied to resolve a well-known Double Seismic Zone in Northern Chile with only data from permanent arrays in the Western United States. We take advantage of array processing techniques to automatically measure pP-P differential arrival times and then combine these measurements into a relative relocation scheme to reduce velocity model biases (Florez & Prieto, 2017). We relocate clusters of 50 to 150 neighboring earthquakes at a time. The set of best fitting relative depths is obtained using the AK135 (Kennett & Engdahl, 1991) global 1-D average velocity model. Initial hypocenters are extracted from the reviewed ISC catalog (Bondar and Storchak, 2011). Typical relative depth errors are of the order of 1 to 2 km.

To apply this technique, we chose narrow and smooth plate segments with as many large intermediate-depth earthquakes as possible (Brudzinski et al., 2007; Nishikawa & Ide, 2014; Ellen M. Syracuse et al., 2010). We sample every major subduction zone and the entire range of plate ages, from 10 to 150 Ma. We avoid triple junctions and zones of highly oblique plate motion. Array processing techniques work effectively when applied to a large number of closely spaced stations; these arrays must be at specific distances from the events to avoid triplications that contaminate the arrivals of interest; pP is cleanly

observed at 30° or more and *sP* is detected between 16° to 19°. We use dense regional networks that have been in operation since at least 2000, mainly in Japan, the western USA, Australia, New Zealand and Taiwan. These criteria limit the number of segments we can study; however careful data selection allows us to analyze 32 slab segments, see Table 3 for a description of the parameters that define them. Each segment analyzed shows a clear DSZ, significant variations in width and depth-extent are readily observed (figure 24). In regions such as Vanuatu, Ryukyu, Philippines, and the Caribbean we were unable to assess the presence of a DSZ, data at the required distance range was not available at the time of this study.

3.3. Double Seismic Zone Characterization

Earlier work by Brudzinski et al. (2007) used global catalogs to statistically assess the presence of a double seismic zone. By taking small segments and rotating their seismicity in the slab down-dip direction, it is possible to test if the obtained pattern can be fit by a bimodal Gaussian distribution, if so, the width of the DSZ is simply estimated as the distance between the Gaussian peaks. Nevertheless, this idea only allows to assert the presence of a DSZ detailed characterization of its geometry and seismicity has relied on local networks located on top of a few slab segments (Kita et al., 2010; Rietbrock & Waldhauser, 2004).

Our new catalog has sufficient depth resolution to systematically explore the factors that control DSZ geometry and to separate seismicity into earthquakes belonging to either the upper or the lower layer. We use a spline interpolation to model the optimal USL and LSL geometry based on earthquake locations, assigning each earthquake to either layer depending on their proximity to each curve (Figure 25). The interpolation is performed

iteratively. First, we calculate an initial DSZ width by fitting a bimodal Gaussian distribution (Brudzinski et al., 2007). Based on this initial width and the location of the two distribution peaks an initial assignment of events is made to either the USL or the LSL given the shortest distance between the event location and each of the splines: if the two distances are within 10% of each other, the event is not assigned to any particular layer; otherwise, it is assigned to the layer corresponding to the nearest curve. Then, the two layers of seismicity are fitted separately using a smoothing spline interpolation. The procedure is performed iteratively until the following two criteria are satisfied: (i) the splines intersect each other at a depth that is within 30 km of the deepest earthquake found in the segment and (ii) the width, measured as the average distance between the two splines (only for the first ¾ of the dipping slab segment) is within 20 % of the initially estimated width. Events are also iteratively assigned to either the USL or the LSL. If after 20 iterations the above-mentioned criteria are not satisfied, the width of the DSZ is set to the initial estimation and no depth-extent measurement is performed for that segment.

We analyze DSZ geometry in terms of two variables: depth-extent and width. The depth-extent corresponds to the depth at which the two splines curves intersect. To determine the width of the DSZ, we estimate the average distance between them in the slab-normal direction (Brudzinski et al., 2007); since the curves typically merge at depth, the width is only estimated using the first 75% of the points in the down-dip direction, to avoid underestimating the width due to the closure of the DSZ. Our results on the width are compared to a bimodal Gaussian fit of seismicity (Brudzinski et al., 2007; Syracuse et al., 2008) with excellent agreement.

Figure 25. Estimation of DSZ width and maximum depth-extend (star) and separation of USL and LSL seismicity (red and black circles) for three segments. **(a)** For the relocated catalog in northern Chile, a smoothing spline is used for fitting the upper and lower seismicity (red and black lines respectively). The maximum DSZ depth or merging depth is defined at the merging point of the two spline curves, and the DSZ width is based on the separation between the upper and lower spline curves. For each slab segment, seismicity is separated in USL and LSL according to the distance to either the upper or lower spline curves. In the case where an earthquake is at a similar distance to either spline, it is undetermined whether it belongs to the USL or LSL (empty circle). **(b)** Similar to (a), for the central America DSZ. **(c)** Similar to (a) for the Japan DSZ. **(d)** Similar to (a) for the Marianas DSZ.

Our relocated catalog provides robust evidence of the ubiquity of DSZ and the strong correlation of DSZ width and plate age (Figure 26), in agreement with previous work (Brudzinski et al., 2007). Indeed, variables such as thermal parameter (Figure 26), arc-trench

distance, and convergence velocity poorly correlate with DSZ width (Figure 28). This is sometimes explained by the depth of hydration of the incoming slab, that is limited by the slab temperature and the stability of hydrated phases (Ranero, 2003). In contrast, the depth-extent is mostly controlled by the thermal parameter (Figure 29). The latter result is similar to that presented for Tonga, and other subduction zones (Wei et al., 2017), estimated by visual inspection of DSZs reported in the literature, and suggests a strongly temperature-controlled mechanism for intermediate-depth earthquakes.
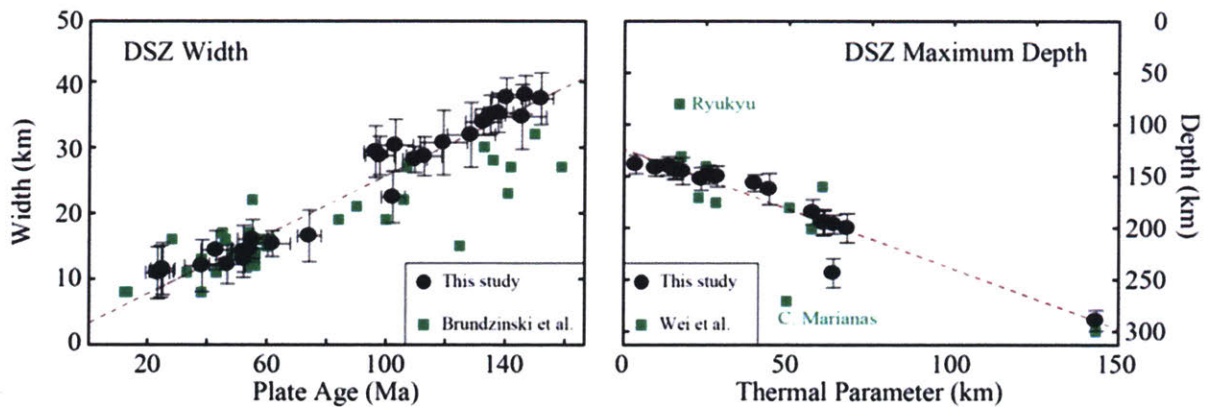
Figure 26. Observed dependence of DSZ characteristics and plate properties at global scales. **(a)** DSZ width is correlated with plate age, similar to previous (green squares) results (Brudzinski et al., 2007), although our estimated values are larger for older plates, which could be explained by the different width determination methods. Our method does not use the earthquakes that are deeper in the region where the USL and LSL merge (Brudzinski et al., 2007). **(b)** the maximum depth of the DSZ (merging point of the USL and LSL) is heavily dependent of thermal properties of the subducting slab. Compiled results (green squares) from various subduction zones (Wei et al., 2017) show a similar behavior to our results. Outliers are marked for the compiled results.

3.4. Frequency-Magnitude Statistics

Counting events may not be the most useful statistical characterization of seismicity, due to variable seismicity productivity, but the relative size among events deserves consideration. We estimate frequency-magnitude statistics independently for the USL and the LSL (Figure 27), for as many different regions as possible (see figures 31 and 32 for details concerning data selection and robustness of calculations). To obtain meaningful and robust statistics we group nearby slab segments and separate events into two categories: those belonging to the USL and those belonging to the LSL. If the total number of events in each one of the two categories exceeds 100 we calculate both b-values by applying a maximum likelihood method (Aki, 1965; Bender, 1983; Wiemer & Wyss, 2000). Our calculation uses the maximum curvature technique to estimate the completeness magnitude (Mc) (Woessner & Wiemer, 2005). We obtain independent b-value measurements for the USL and the LSL in as many different regions as possible (figure 27). The age of each region is simply computed as the arithmetic average of the ages of the segments it contains.

We consistently find that the USL has significantly larger b-values than the LSL. USL b-values positively correlate with plate age, resembling the strong correlation between age and b-value found for shallow subduction zone earthquakes (Nishikawa & Ide, 2014). In contrast, b-values remain mostly constant for the LSL, with an average of about 0.8. Previous studies have found large b-value anomalies near the top of some slab segments (Katsumata, 2006; van Stiphout et al., 2009; Wiemer & Benoit, 1996; Wyss et al., 2001); our results suggest that these differences are systematic, may be controlled by a few physical parameters, and

are a global feature. Recent work in Japan (Kita and Ferrand, 2018) show larger b-values in Hokkaido along the USL, but have lower b-values in the Tohoku area. Our results do not have the resolution to be able to compare each segment within subduction zone due to the less complete global catalogs, but point towards a global systematic behavior of b-values between USL and LSL.

The number of events used to estimate the b-value for each region is relatively small, although similar numbers have been used to study frequency-size statistics (Woesner and Weimer 2005, Schorlemmer et al., 2005, Nishikawa & Ide, 2014). We evaluated the statistical significance of the estimated USL and LSL b-values differences, using a t-test (Pacheco et al., 1992, Andrade et al., 2014) and can reject the hypothesis that the two b-values are the same with a 0.998 confidence (see section 6 for details). Figure 35 shows a global comparison of the frequency-size statistics of USL and LSL seismicity, and their ratio, confirming that the observed differences are significant.
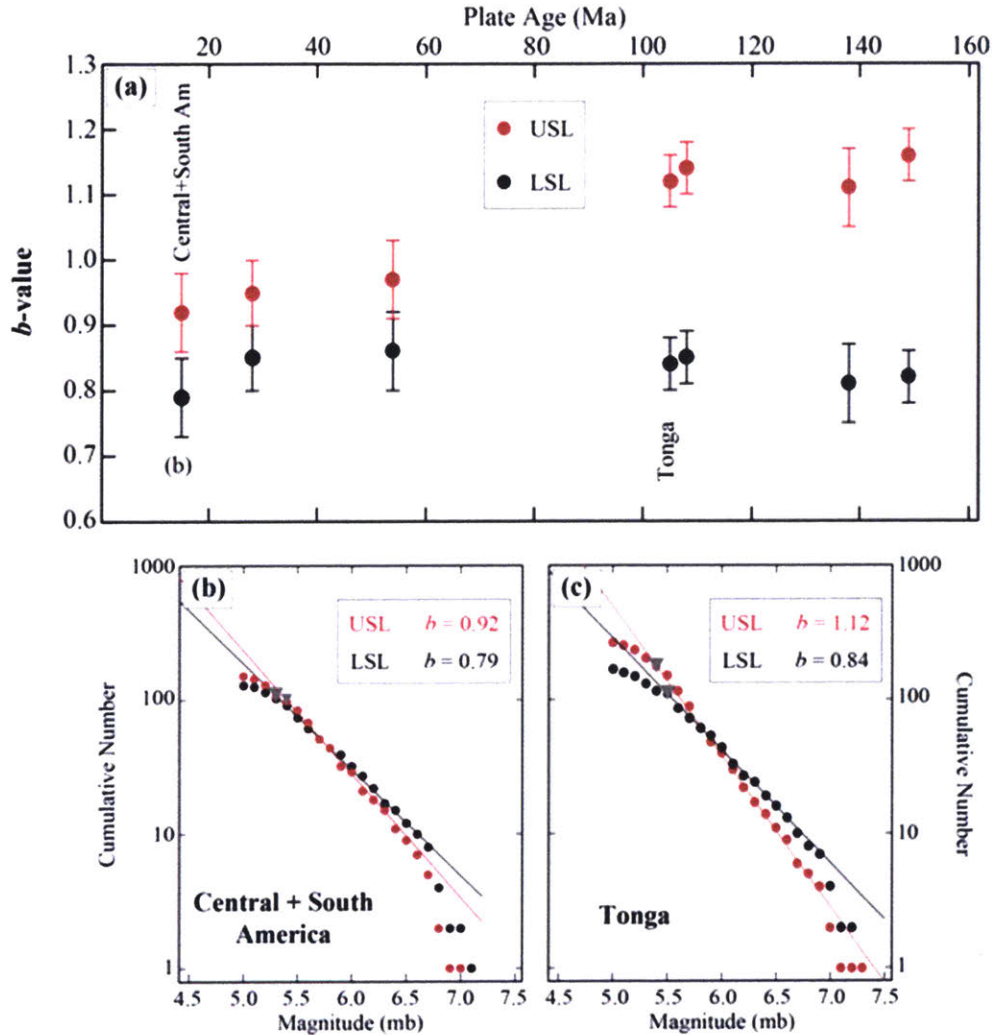
Figure 27. b-value differences between upper and lower DSZ layers. (a) Estimated b-values and bootstrap errors for the USL and LSL as a function of plate age. In some cases, slab segments of similar age are combined to obtain a robust estimate. (b) Frequency-magnitude distribution for events in Central and South America, for the USL (red dots) and the LSL (black dots). Gray triangles represent Mc. Red and black lines represent the slope or b-value estimated. (c) Same is (b) for the Tonga slab segment.

3.5. Independent Validation

The precision and robustness of the applied relative relocation technique (see Figure 31 for examples illustrating some of our results) are studied in chapter 2; however, before calculating Frequency-Magnitude statistics we have to robustly split events into two groups: those belonging to the USL and those that belong to the LSL. We start by studying the

sensitivity of this assignment to the input parameters of the relocation algorithm. We test the most extreme of the scenarios: different epicenters and starting depths for the same set of earthquakes. All the results presented thus far use the reviewed ISC catalog (Bondar and D. Storchak, 2011) to select events and their corresponding hypocenters. To perform the desired test a global catalog of similar quality, built using compatible assumptions and spanning the same time interval must be used; such a dataset did not exist until the release of the ISC-EHB bulletin (Bondar and D. Storchak, 2011), considered to be slightly more accurate than the ISC (Engdahl et al., 1998).

The ISC-EHB catalog uses more stringent data selection criteria, so it does not contain all events used in this study (Centre, 2018; Engdahl et al., 1998). For the regions of Tonga and Kurile we were able to find a large number of earthquakes with both ISC-EHB and reviewed ISC hypocenters. Figure 32 shows the results for one segment in each region. For the section in Tonga, the initial hypocenters have no impact on the event groupings. For Kurile segment, two earthquakes that originally located to the LSL are assigned to the USL. Their relatively small magnitudes, Mb 5.4 and Mb 5.5, would not significantly impact the Frequency-Magnitude statistics. We performed the same analysis in 8 different segments in Tonga, Kurile, and Izu-Bonin. In the worst of cases, no more than five earthquakes were assigned to a different seismicity layer, and their magnitudes never exceed Mb 5.6; suggesting that our results are not sensitive to the choice of initial hypocentral parameters.

Incorrectly assigned magnitudes also have the potential to bias our conclusions. Our statistical calculations use body wave magnitudes (Mb) as reported by the ISC (Centre, 2015). We use the Global Centroid Moment Tensor (GCMT) catalog (Ekstrom et al., 2012)

to assess their reliability. GCMT uses a moment magnitude scale (M_W). Body wave magnitudes, like many other local magnitude estimates, saturate for large earthquakes; after a given threshold all earthquakes are assigned the same magnitude. Examination of Figure 33 shows a clear linear relationship between Mb and MW for all relocated events that were also present in the GCMT catalog, no signs of scale saturation are observed.

As discussed before, a meaningful b-value estimation requires a sufficiently large number of events (at least a 100 were used in all of our calculations). The GCMT catalog magnitude of completeness is typically around M_W 5.4, so using it to study spatial variations in b-values is not often possible. For the regions of Tonga and Kurile, we were able to separately quantify frequency-magnitude statistics for USL and LSL, using M_W (Figure 34). The results are consistent with those obtained using Mb. In Tonga, a b-value of 1.09 was found for the USL. As expected the estimates using different magnitude scales do not completely agree, a smaller number of events is used in the MW statistics; however, significant differences in b-values for USL and LSL persist. It is unlikely that our observations are biased by either the magnitude scale or the initial hypocentral parameters used for event relocation.
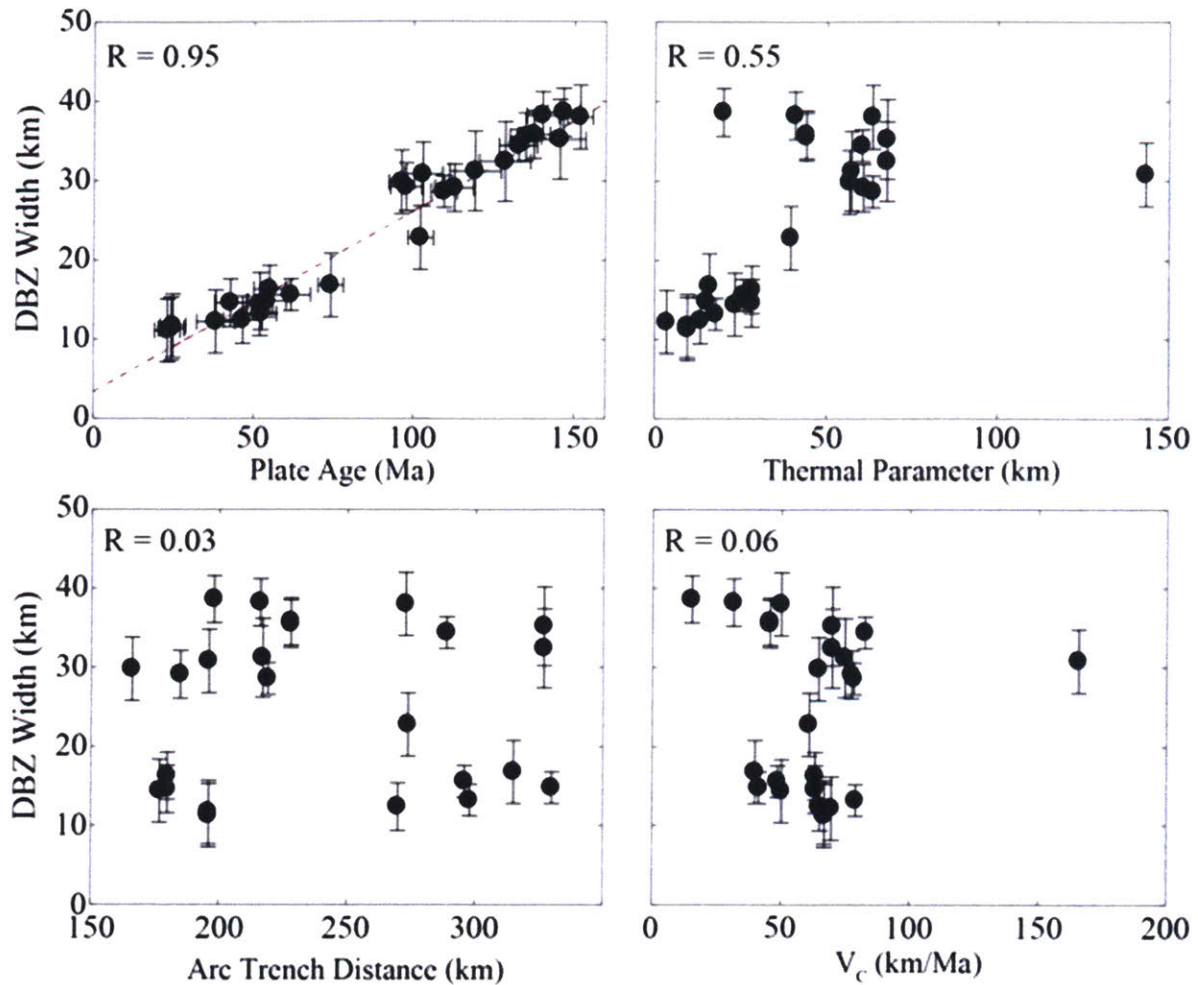
Figure 28. Comparison of tectonic properties and DSZ width. **(a)** Relationship between plate age and DSZ width. Dashed line shows the linear regression line and corresponding R2 value. **(b)** Relationship between thermal parameter and DSZ width. **(c)** Relation between Arc-trench distance and width. **(d)** Relationship between plate velocity and DSZ width. The DSZ width is best correlated with Plate age (Engdahl et al., 1998), the correlation with thermal parameter is less clear.
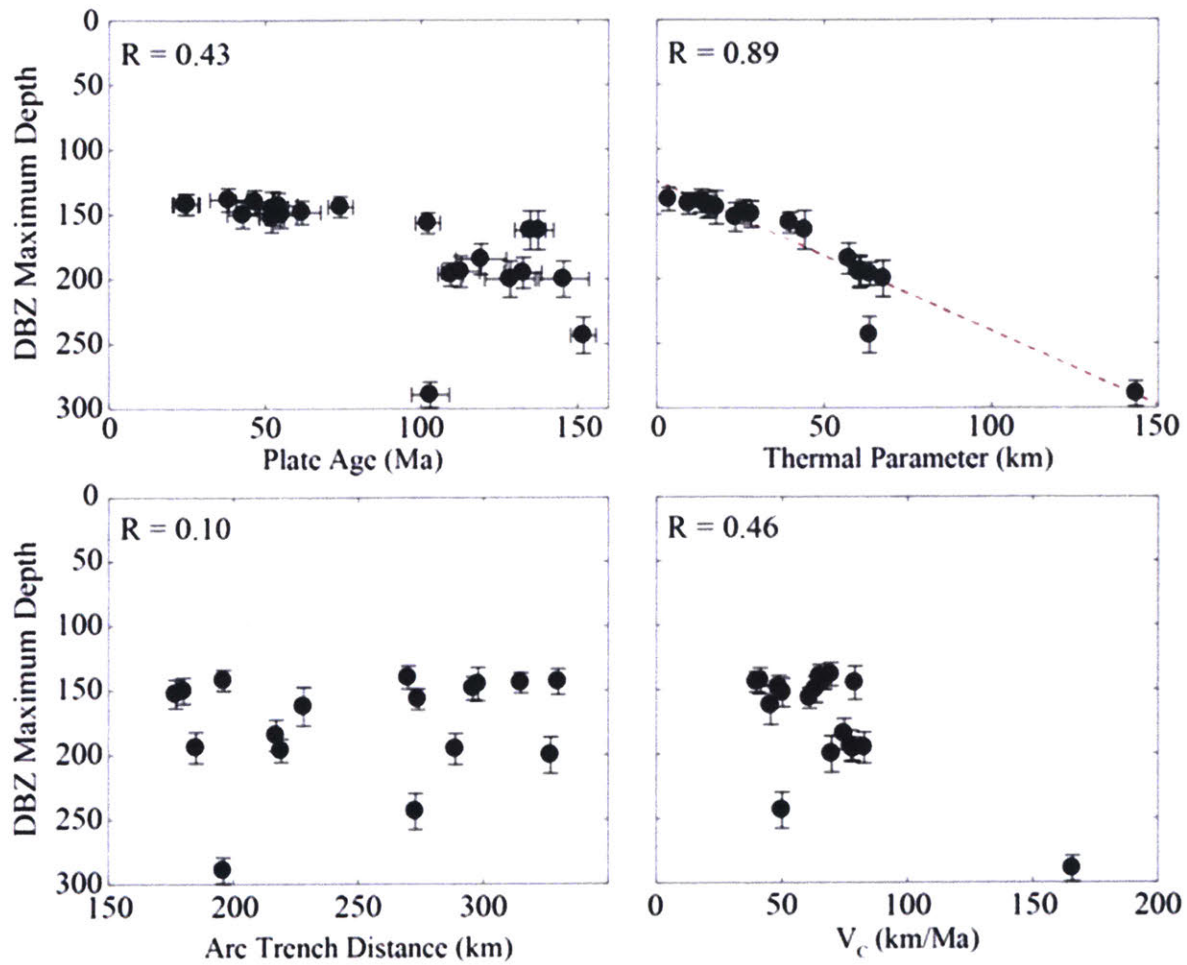
Figure 29. Comparison of tectonic properties and the maximum depth of the DSZ. **(a)** Relationship between plate age and maximum depth. **(b)** Relationship between thermal parameter and DSZ depth extent. Dashed line shows the linear regression line and corresponding R2 value. **(c)** Relation between Arc-trench distance and depth extent. **(d)** Relationship between plate velocity and DSZ depth extent. The DSZ depth extent is best correlated with thermal parameter, the correlation with plate age is less clear.
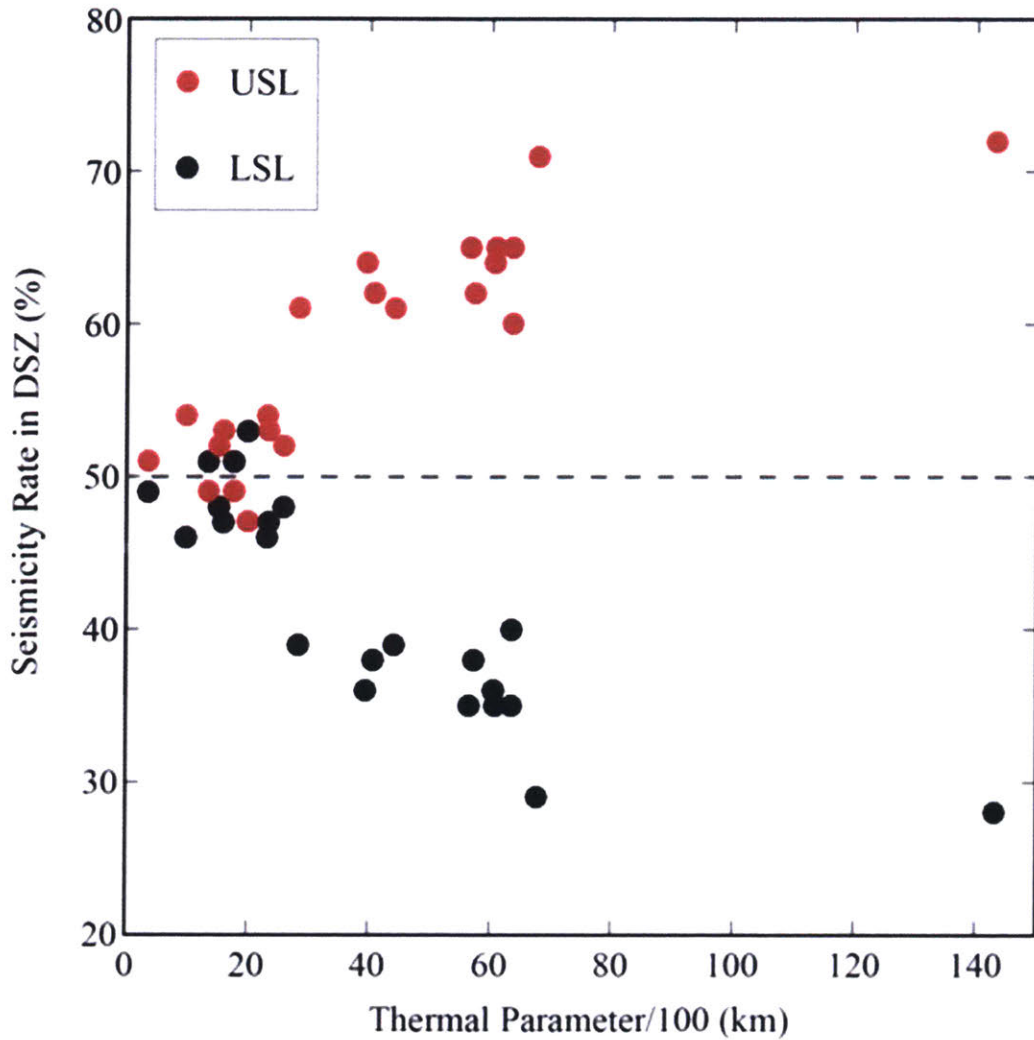
Figure 30. Relative seismicity rate in the USL and LSL as a function of thermal parameter. Seismicity rate describes the number of events per year above Mb 5.0 in our catalog.
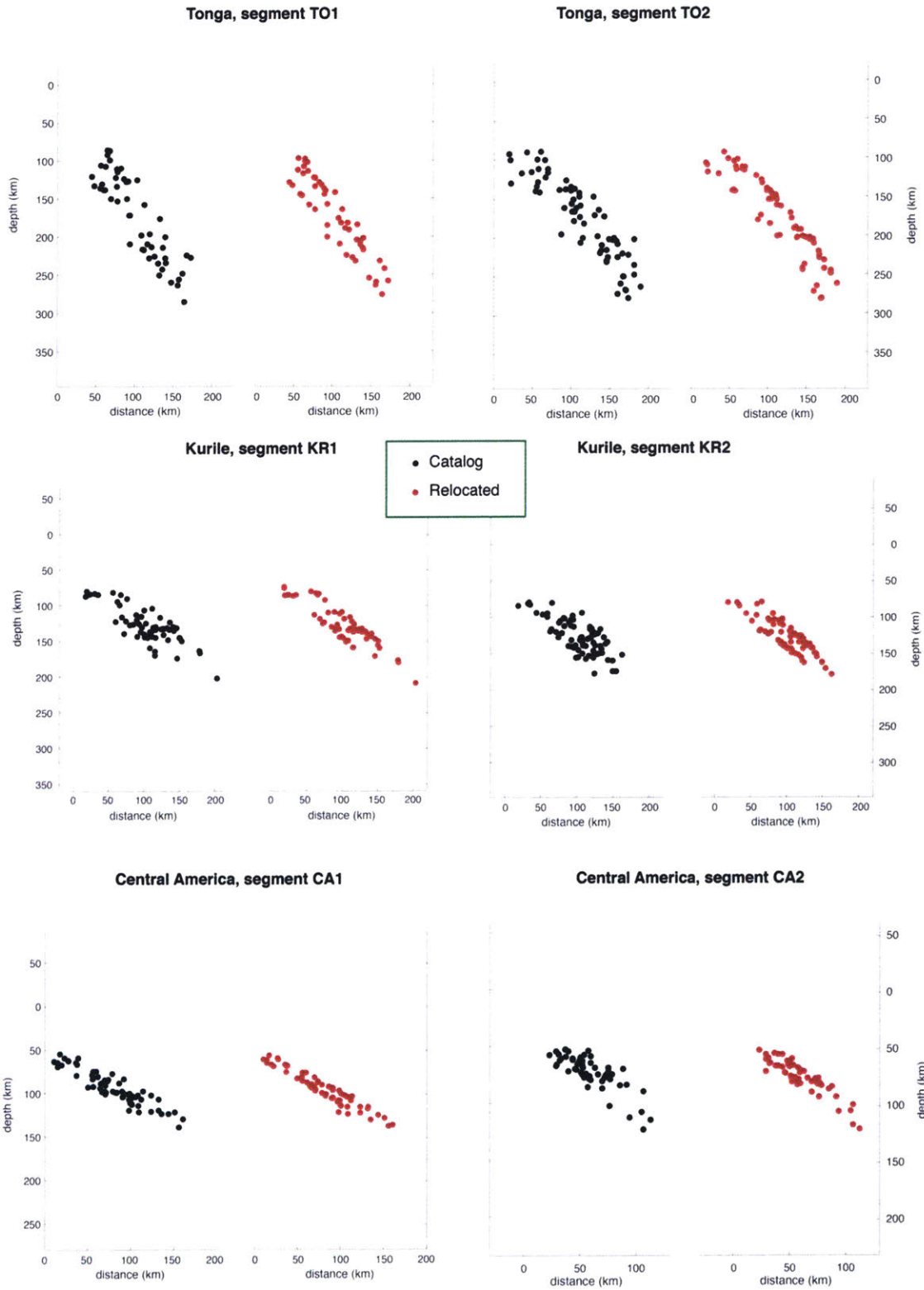
Figure 31. Comparison between Catalog and relocated events for segments in Tonga, Kurile, and Central America.
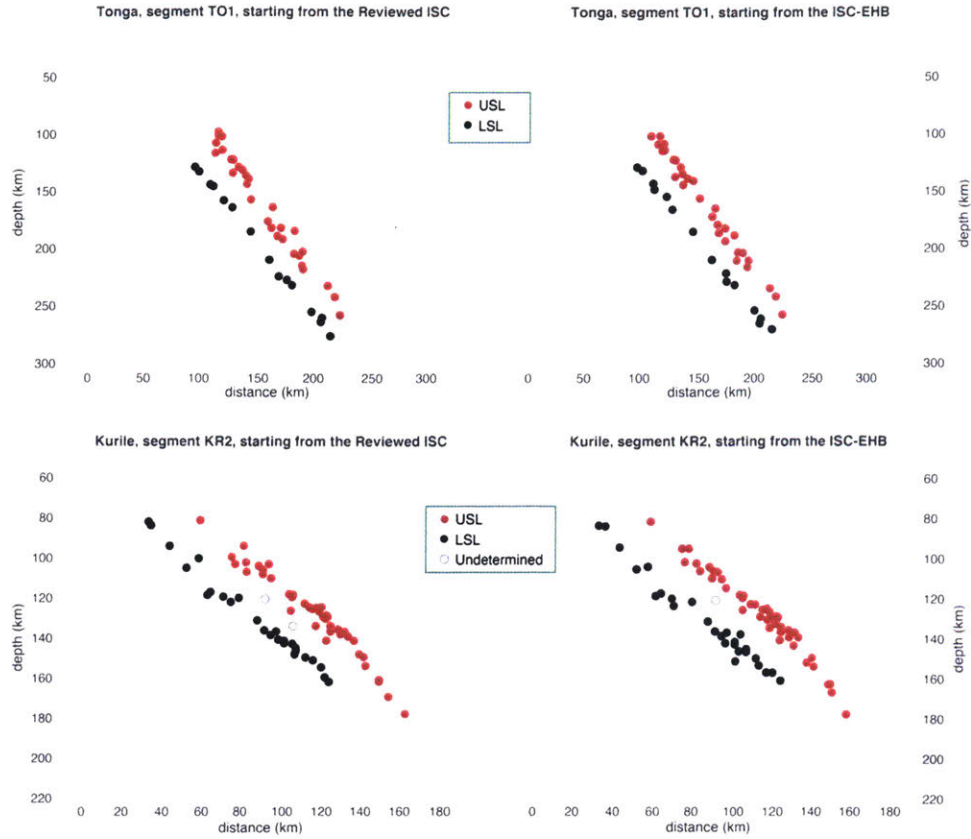
Figure 32. Comparison of resulting relocations when starting epicenters and depths are taken from either the reviewed ISC catalog or the ISC-EHB catalog. Results for two segments are shown, one in Tonga, and the other in Kurile.
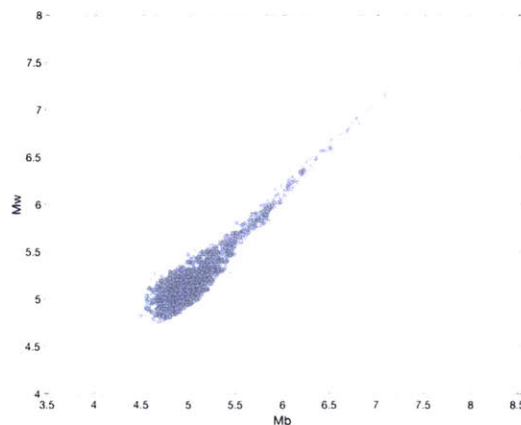
Figure 33. Result for all events used in this study. Cross-plot of body wave magnitude (Mb), as reported by the ISC, and Moment Magnitude (MW) taken from the GCMT catalog. Events without an assigned MW are not plotted. A linear trend emerges; no sign of scale saturation is observed.
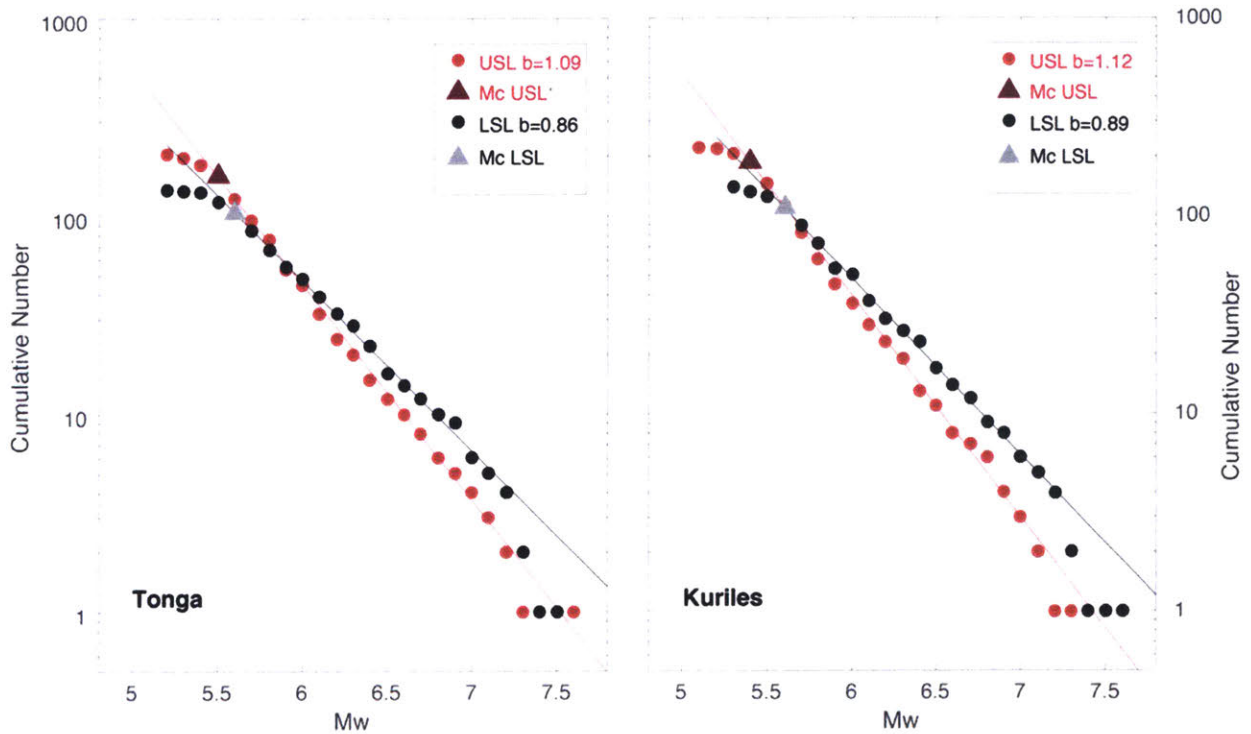
Figure 34. Frequency-magnitude statistics for Tonga and Kurile regions using moment magnitude scale. Starting epicenters and depths are from the ISC-EHB catalog (Centre, 2018). All magnitudes (MW) are taken from the GCMT catalog. If an earthquake has no reported magnitude it is not included in the statistics.

3.6. Statistical Analysis

In all the regions analyzed we quantify b value uncertainties by a applying a bootstrap resampling scheme (Woessner & Wiemer, 2005). For each region we generate $N = 1000$ bootstrap samples. Each bootstrap sample is a new catalog, generated by drawing M events with replacement from the original catalog, where M is the total number of events in the

76

region. For each sample we calculate both M_c and b. The result of this procedure is a distribution of values for b with mean $< b >$ and standard deviation σ. We report $< b >$ as our preferred b-value estimate for the region and 2σ as a conservative error measurement.

We evaluate the robustness of the average systematic global difference in b-values by applying a t-test (Pacheco et al., 1992; Andrade et al., 2014). Let $H0_1$ be the null hypothesis: $b_{USL}-b_{LSL}=0$, which states that the average b-value for the USL is equal to the average b-value for the LSL. In this scenario we test for differences in the average b-values of the USL and LSL. By running a t-test we reject $H0_1$ with 99.8% confidence. Now, let $H0_2$ be: $b_{USL}-b_{LSL}<0$. To run this test, we use a one-sided distribution and again reject $H0_2$ with 99.8% confidence. We therefore assert, with high statistical confidence, that the average b-value for the USL is larger than the one for lower layer. In practice, H0 is defined as $b_{USL} \leq b_{LSL}$, so a single statistical test suffices. We also perform a Wilcoxon's Rank-Sum statistic, more robust against non-normal distributions (Blair et al., 1980; Paternoster, 1998; Fay et al., 2010), which confirms that we can reject the null-hypothesis with at least 99.8% confidence

We then perform an individual Student's t-test for each region analyzed. We test for differences in slope, as in Andrade et al. (2014). We use the uncertainties in the individual USL and LSL b values. For each region we let H0 be $b_{USL} \leq b_{LSL}$. Table 1 summarizes our results.

Section	Average Age (Ma)	Confidence H0 is rejected
Central America	15	0.915
New Britain	28	**0.894**
Sumatra	54	**0.889**
Tonga	105	0.999
Kuriles	108	0.999
Izu-Bonin	138	0.999
Marianas	149	0.999

Table 1. Confidence level that the null-hypothesis ($b_{USL} \leq b_{bLSL}$) is rejected by comparing the b-values of the upper and lower layers in each section using a Student's t-test. In red, those section where confidence is lower than 90%.

In general, for younger plates, where the b-values are similar (visually their error bars overlap or almost overlap), the confidence that $b_{USL} > b_{LSL}$ is lower than for older plates where these b-values are significantly different (the error bars do not overlap). Nevertheless, as It was shown by combining data for all regions, the main conclusion of the paper is quantifiably robust.

3.7. Sample Size Considerations

It is always desirable to have a large sample size when frequency-size distributions are studied, unfortunately when detailed b-value mapping is needed (Woesneer & Weimer, 2005) or global comparison are performed (Nishikawa & Ide, 2014) analyses must rely on relatively small samples, usually no larger than 300 earthquakes. Following work by

Nishikawa & Ide (2014), we have restricted our study to regions with $N_{EQ} \geq 100$, where N_{EQ} is the total number of earthquakes in the region's dataset. Table 2 contains the total number of earthquakes, N_{EQ}, for each of the regions and provides counts of the number of events with magnitude equal or larger than the corresponding magnitude of completeness.

Section	Average Age (Ma)	USL		LSL	
		N_{EQ}	$N_{EQ} > M_C$	N_{EQ}	$N_{EQ} > M_C$
Central America	15	159	98	129	102
New Britain	28	118	84	112	76
Sumatra	54	101	41	100	39
Tonga	105	272	178	184	110
Kuriles	108	341	242	208	138
Izu-Bonin	138	101	72	102	64
Marianas	149	101	54	102	38

Table 2. Number of events used in estimating b-values shown in Figure 27 of the paper. NEQ is the total number of earthquakes used for each region.

To evaluate the main conclusion of the paper with a substantially larger sample size we can combine the data for each individual region into two larger datasets: earthquakes that are located in USL and earthquakes in the LSL (Figure 25). We are not particularly concerned with the absolute b-values of each dataset, rather we follow a simple mathematical procedure to demonstrate that the difference in slopes is robust. A commonly used and useful form of the frequency-size distribution is given by:

$$\log(N) = a - bM$$

where N is the cumulative number of earthquakes with magnitude larger than M and b is the slope of the distribution. To compare two magnitude-size distributions, instead of fitting the datasets individually, we can fit the difference in slopes by looking at the ratio of the cumulative number of earthquakes. Let b_{up} be the b-value for the USL and b_{down} be the b-value for the LSL:

$$\log(N_{up}) - \log(N_{down}) = (a_{up} - b_{up}M) - (a_{down} - b_{down}M)$$

$$\log\left(\frac{N_{up}}{N_{down}}\right) = (a_{up} - a_{down}) - (b_{up} - b_{down})M$$

Where $b_{up} - b_{down}$ represent the difference in slopes or b-value difference. We apply this simple procedure to the combined datasets shown in figure 35. A Maximum Likelihood Estimation yields $b_{up} - b_{down} = 0.34 \pm 0.19$. The absolute value may not be as important as the positive sign is reliable.
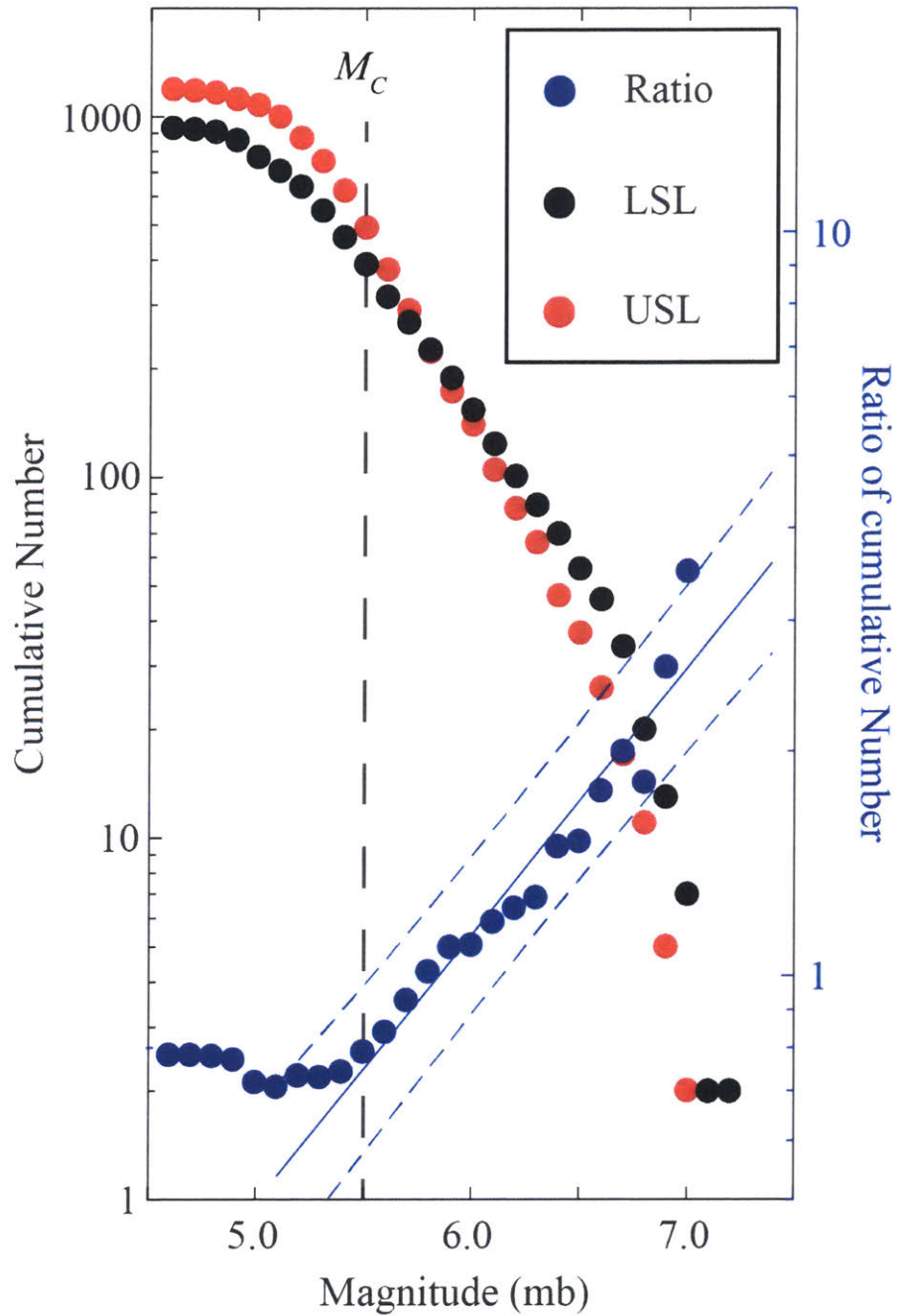
Figure 35. In red, combined dataset of events that locate to the Upper Seismic Layer. In black, combined dataset of earthquakes that locate to the Lower Seismic Layer. In blue, relative frequency-size distribution capturing the difference in slopes between the two layers.

Chapter 4.

4. Conclusions

4.1. Teleseismic earthquake relocation using depth phases

We have proposed a technique that significantly reduces the uncertainties associated with relative depth determination for earthquakes observed at teleseismic distances. This has been achieved by using subarrays to systematically measure pP-P times. We have shown that such measurements exhibit some of the properties of station level measurements (Richards-Dinger and Shearer, 2000). In particular, many subarray level measurements show systematic deviations from model predictions (Figure 8), resembling source-specific terms (Richards-Dinger and Shearer, 2000). By computing the difference between pP-P times for pairs of events whose rays' sample similar paths, we minimize errors due to unmodeled velocity heterogeneity (Waldhauser and Ellsworth, 2000). The combination of these ideas into a single coherent procedure enabled us to reduce relative depth uncertainties down to about 1.5 km. Also, we have no tradeoff between depth and origin time, as it is typically the case for most relocation schemes (Lin and Shearer, 2005).

This technique allowed us to determine the rupture plane of a large intermediate-depth earthquake, by precise relocation of its largest aftershocks. But more importantly, we have shown that by improving the precision of relative earthquake depths it becomes possible to clearly resolve the geometrical structure of Double Seismic Zones. The results from applying this method to intermediate-depth earthquake location gave us new insights into the physical mechanism of intermediate depth earthquakes.

The main limitation of our relocation strategy is the availability of data at the required distance ranges between 30°-90° for the pP phase. Events need to be large, typically M > 5.0, so that the pP-P time can be measured on the Vespagrams. New stacking techniques (Korenaga, 2013) would certainly allow us to include earthquakes with smaller signal-to-noise ratio. However, analysis of the sP phase, observed at distances between 8° and 15°, seems like a promising future area of research, it would open the possibility of relocating smaller magnitude and thus larger sets of events.

4.2. Double Seismic Zone Geometry

The geometrical structure of Double Seismic Zones is controlled by the physical properties of the subducting slab. Plate age shows a strong positive correlation with DSZ width and the slab's thermal parameter correlates well with the maximum depth of seismicity along the DSZ. Variables such as arc-trench distance and slab convergence rate did not show a statistically meaningful correlation with any of the variables that define geometry. We note that in a few segments the relative number of earthquakes that locate 20 to 30 km up-dip of the maximum depth is small, potentially less that 10% of the total number of events, so maximum depth errors might have been underestimated. However, we believe that the general trend observed is robust. Compiled maximum depths analyzed using local catalogs (Wei et al., 2017) provide similar estimates to the ones shown in this work.

4.3. Seismicity along Double Seismic Zones

Our ability to clearly define DSZ geometry allows us to assign earthquakes to either the USL or the LSL with little ambiguity. A few studies (Korenaga, 2017; Wei et al., 2017)

suggest that seismicity rate— the number of earthquakes per year—is considerably smaller in the lower layer, as compared to the upper. Our results provide a partial explanation for this observation: the slab's thermal parameter exerts an important control on relative seismicity rates. Colder subducting plates show higher rates for their USL, e.g. Tonga, a cold and rapidly converging slab, has a lower layer with a surprisingly small number of earthquakes (Wei et al., 2017). Warmer slabs display roughly equal rates for both planes. This issue deserves further investigation using local catalogs with smaller completeness magnitudes.

Previous studies have shown that high *b*-values anomalies correlate well with regions where dehydration reactions are expected (Wiemer & Benoit, 1996; Wyss et al., 2001) or with fracture zones where abundant fluids are present (Schlaphorst et al., 2016); therefore, *b*-values along subduction zones provide an indirect assessment of fluid content. A relatively dry lithospheric mantle (lower layer) may explain the consistently smaller *b*-values observed regardless of subducting plate age, thermal parameter or composition. This has important implications for the mechanism of intermediate-depth earthquakes, thought to occur as the consequence of a series of dehydration reactions (Hacker et al., 2003; Kirby, 1995; Yamasaki & Seno, 2003).

Dehydration-induced fluid overpressure would be consistent with the higher *b*-value observed in the USL but very unlikely to play a significant role in the triggering of lower layer seismicity (Chernak, 2011; Hilairet et al., 2007; Proctor & Hirth, 2015; Reynard et al., 2010; Zhang et al., 2004). Our results suggest a relatively dry lithospheric mantle hosting intermediate-depth earthquakes, in agreement with recent field observations (Scambelluri et

al., 2017) and deformation experiments on relatively dry synthetic antigorite-olivine aggregates at upper mantle conditions (Ferrand et al, 2017).

Our results provide new and robust constraints on the physical mechanism responsible for triggering intermediate depth earthquakes. Whatever the details of the processes might be, the mechanism responsible for LSL earthquakes is fundamentally different from the one operating in the USL.

4.4. A Possible Mechanism for Lithospheric Mantle Earthquakes

We propose a conceptual mechanism for LSL earthquakes. Any viable mechanism must explain the three stages of earthquake rupture: Initiation, fracture propagation and arrest. As discussed in the previous section dehydration-embrittlement is inconsistent with our observations and with recent field (Scambelluri et al., 2017) and experimental evidence (Ferrand et al, 2017). An alternative would be a self-localizing thermal run-away mechanism (Keleman and Hirth, 2007; John et al., 2009; Prieto et al., 2013). But we do not favor this model because it does not explain rupture arrest and the conditions under which it operates are too restrictive (e.g., Karato et al., 2001).

We posit that LSL earthquakes results from the interplay of two physical mechanisms: Dehydration Driven Stress Transfer DDST (Ferrand et al, 2017) and Localized Heating LH (Ohuchi et al., 2017). DDST would be responsible for earthquake initiation, but once the fracture nucleates localized heating drives rupture propagation, until it arrests. The earthquake initiation would occur in a near-anhydrous lithospheric mantle, maybe due to stress transfer after dehydration of a nearby hydrated mantle (Scambelluri et al., 2017;

Ferrand et al., 2017). This is quite different from the mechanism that is expected in the USL, where the lithosphere is expected to be hydrated. Then LH would take over, allowing the rupture to propagate over large distances.

4.5. Other differences observed in DSZ seismicity

We have shown differences in the behavior of seismicity in the upper and lower layers along DSZs, in particular magnitude-frequency distributions. These observations suggest that the mechanism associated with the generation LSL earthquakes is different from the one operating in the USL.

One such parameter is the rupture characteristics of earthquakes in the USL and LSL. Kita and Katsumata (2015) analyzed the source parameters in Hokkaido along the USL and LSL and suggest that there are slight but statistically significant differences between the stress drops of earthquakes in both layers. This is confirmed by Chu et al. (2019), where they see differences in both stress drops and apparent stress from earthquakes in the USL and LSL in Hokkaido. In contrast, the radiation efficiency is similar in both layers. If the mechanism responsible for intermediate-depth earthquakes is a thermal shear run away for the LSL, we would expect both stress drops and radiation efficiency (Prieto et al., 2013) to differ from those in the USL. A more complete and global analysis of earthquake source parameters is needed to confirm differences along DSZ.

The aftershock behavior of intermediate-depth earthquakes remains puzzling. Persh and Houston (2004) found that in global catalogs the aftershock productivity of events located between 100 km and 300 km depth is at least a factor of 10 smaller than the one of shallower

events and about half the productivity of the deepest earthquakes (depth > 550 km). Unfortunately, their study is hindered by the relatively small magnitude of completeness of global catalogs, which varies across regions but is typically larger than Mw 4.5. Also, all earthquakes were placed into fixed depth bins, regardless of their tectonic environment, resulting in a global average that makes it hard to tell apart significant statistical contrasts across regions. All work (Kagan and Knopoff 1980; Prozorov and Dziewonski 1982; Frohlich 1987) based on the ISC global seismicity catalog, which has a completeness magnitude of about Mw 4.0, supports Persh and Houston's conclusion: aftershocks are less common for events between 100 km and 450 km depth (Kagan and Knopoff 1980; Prozorov and Dziewonski 1982; Frohlich 1987). However, detailed analysis of the October 2015 Hindu Kush Mw 7.5 (Li et al., 2018) earthquake revealed an abundant aftershock sequence. Li et al. (2018) used modern waveform matching techniques to detect about 3000 in a period of 35 days after the main shock, while the ISC catalog only recorded 198 aftershocks for the same period of time (Li et al., 2018). Therefore, drawing meaningful conclusions about the aftershock behavior of intermediate-depth earthquakes requires the analysis of dense local seismicity catalogs with smaller completeness magnitudes.

We take advantage of three state-of-the-art seismicity catalogs to perform a preliminary characterization of aftershock behavior for intermediate-depth seismicity. We analyze two subduction zones: Northeast Japan and Northern Chile (Figure 36), which represent end members in terms of age and thermal parameter. Intermediate-depth earthquakes in Northeast Japan are clustered along a DSZ with a relatively cold-core and a width of about 30 km (Figure 36). In Northern Chile, seismicity is also clustered along two planes, but the slab is younger and the DSZ width is 12-16 km (Figure 36). We extract mainshocks and their

hypocentral information from the global catalog generated in this thesis. Our dataset is optimized for mapping the geometrical structure of DSZ and it is constrained by depth phases, so we use it to unambiguously assign events to either the USL or the LSL, as discussed in section 3.3. The aftershocks on the other hand are extracted from two dense local catalogs: the JAM for northeast Japan and the Sippl et al. (2018) catalog for Northern Chile. By merging well-constrained hypocentral information for mainshocks with dense local seismicity we are able to separately study the aftershock behavior for the USL and LSL.
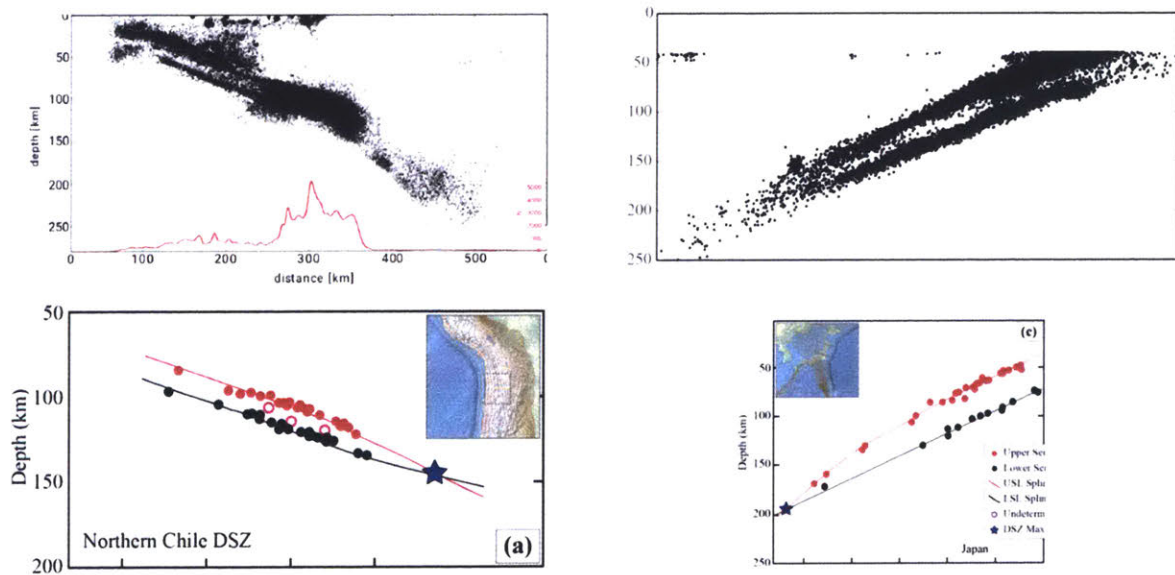
Figure 36. Double Seismic Zones in Chile and Japan constrained by both dense local seismicity catalogs and our relocated global catalog.

Upper Seismic layer earthquakes develop clear and abundant aftershock sequences, similar to those observed for shallow earthquakes. LSL events are consistently less productive. Productivity is measured as the number of aftershocks in a window of five days after the mainshock and is normalized by mainshock magnitude (Persh and Houston, 2004),

88

earthquakes in the USL produce 3 to 4 times more aftershocks than those in the LSL (Figure 39). This observation holds in both Chile (Figure 37) and Japan (Figure 38), two rather different subduction zones, so we posit that, again, this points towards a fundamental difference in the triggering mechanism of intermediate-depth earthquakes.
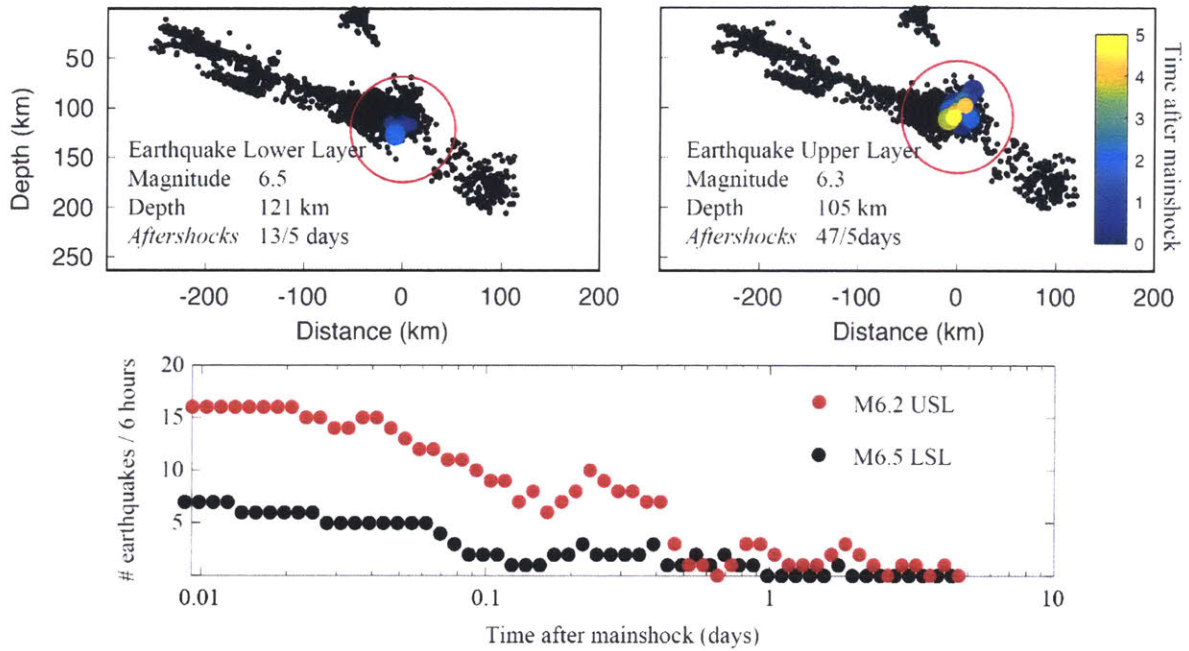
Figure 37.Comparison of USL and LSL aftershock sequences for Chile.
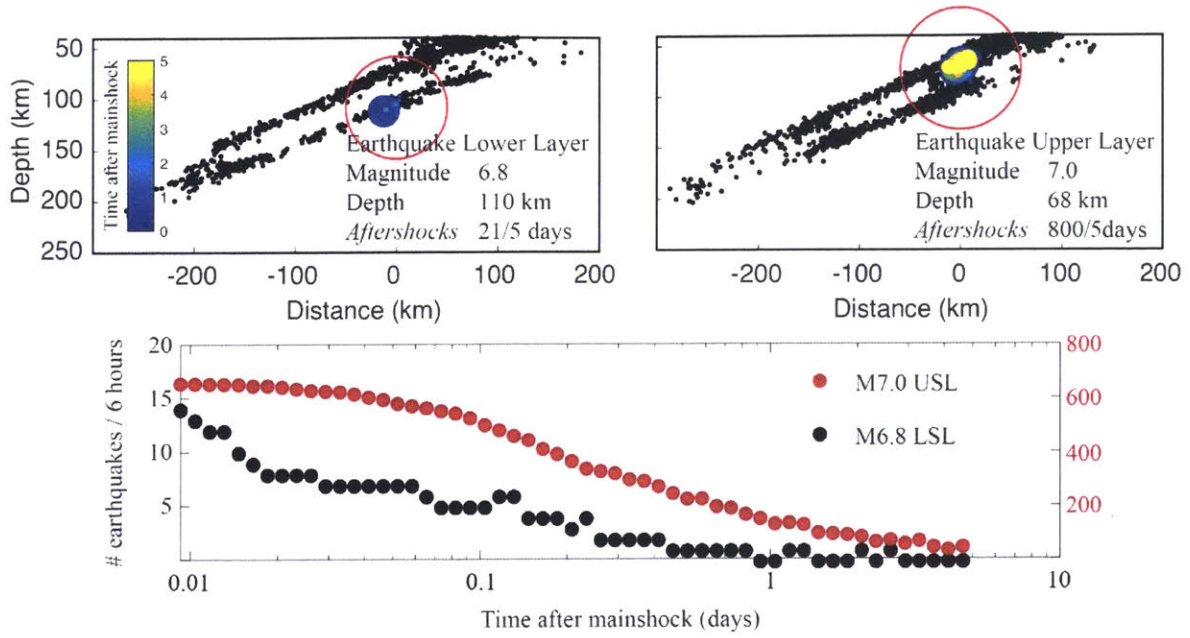
Figure 38. Comparison of USL and LSL aftershock sequences for Northeast Japan.
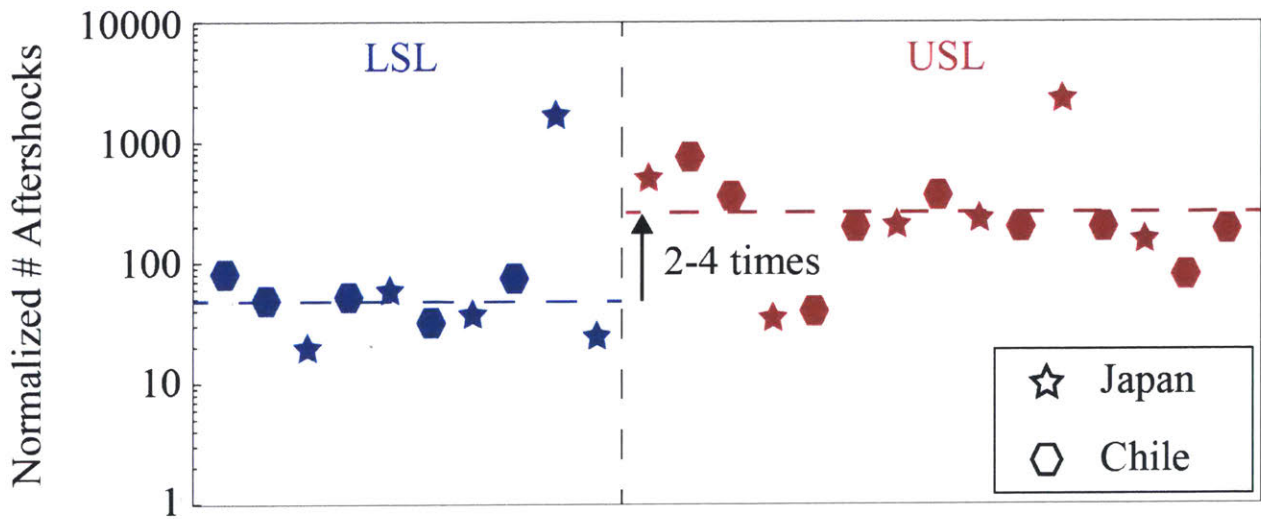
Figure 39. Normalized aftershock productivity for both Chile and Japan.

References

Aki, K. (1965), Maximum likelihood estimate of b in the formula log n = a -bm and its confidence limits. Bull. Earthquake Res. Inst. Univ. Tokyo, 43, 237-239.

Andersen, T. B., K. Mair, et al. (2008). "Stress-release in exhumed intermediate-deep earthquakes determined fromultramafic pseudotachylyte." Geology 36: 995-998.

Andrade, J. M., & Estévez-Pérez, M. G. (2014). Statistical comparison of the slopes of two regression lines: a tutorial. Analytica chimica acta, 838, 1-12.

Aster, R. C., B. Borchers, and C. H. Thurber (2005), Parameter Estimation and Inverse Problems, *Int Geophys Ser*, *90*, 1-303.

Blair, R. C., & Higgins, J. J. (1980). A comparison of the power of Wilcoxon's rank-sum statistic to that of student's t statistic under various nonnormal distributions. Journal of Educational Statistics, 5(4), 309-335.

Blair, R. C., & Higgins, J. J. (1980). A comparison of the power of Wilcoxon's rank-sum statistic to that of student's t statistic under various nonnormal distributions. Journal of Educational Statistics, 5(4), 309-335.

Bondár, I., and D. Storchak (2011), Improved location procedures at the International Seismological Centre, *Geophysical Journal International*, *186*(3), 1220-1244, doi:10.1111/j.1365-246X.2011.05107.x.

Böse, M., V. Sokolov, et al. (2009). "Shake Map Methodology for Intermediate-Depth Vrancea (Romania) Earthquakes." Earthquake Spectra 25: 497-514.

Burrman, V. S. and P. Molnar (1993). "Geological and geophysical evidence for deep subduction of continental crust beneath the Pamir, Spec. Pap." Geol. Soc. Am. 281: 1-75.

Brudzinski, M. R., C. H. Thurber, B. R. Hacker, and E. R. Engdahl (2007), Global prevalence of double Benioff zones, *Science*, *316*(5830), 1472-1474, doi:10.1126/science.1139204.

Cassidy, J. F., and F. Waldhauser (2003), Evidence for both crustal and mantle earthquakes in the subducting Juan de Fuca plate Geophysical Research Letters Volume 30, Issue 2, *Geophysical Research Letters, 30*(2), n/a.

Carr, M. J. and R. E. Stoiber (1973). "Intermediate depth earthquakes and volcanic eruptions in Central America, 1961-1972." Bulletin Volcanologique 37: 326-337.

Centre, I. S. (2015). On-line Bulletin. *Internatl. Seismol. Cent.*

Centre, I. S. (2018). ISC-EHB Bulletin. *Internatl. Seismol. Cent.*

Chatelain, J. L., S. W. Roecker, et al. (1980). "Microearthquake seismicity and fault plane solutions in Hindu Kush region and their tectonic implications." J. Geophys. Res. 85: 1365-1387.

Chernak. (2011). Syndeformational antigorite dehydration produces stable fault slip. *Geology, 39*(9), 847-850. http://dx.doi.org/10.1130/G31919.1

Chollet, M., I. Daniel, et al. (2009). "Dehydration kinetics of talc and 10 Å phase: Consequences for subduction zone seismicity." Earth Planet. Sc. Lett. 284 57-64.

Christeson, G. L., P. Mann, et al. (2008). "Crustal structure of the Caribbean–northeastern South America arc-continent collision zone." J.Geophys. Res. 113(B08104).

Cortes, M. and J. Angelier (2005). "Current states of stress in the northern Andes as indicated by focal mechanisms of earthquakes." Tectonophysics 403: 29-58.

Csontos, L. (1995). "Tertiary tectonic evolution of the Intra-Carpathian area: a review." Acta Vulcanologica 7 (2): 1-13.

Davison, A. C., and D. V. Hinkley (1997), *Bootstrap methods and their application*, x, 582 p. pp., Cambridge University Press, Cambridge ; New York, NY, USA.

DeMets, C., R. G. Gordon, D. F. Argus, and S. Stein (1990), Current plate motions Geophysical Journal International Volume 101, Issue 2, *Geophysical Journal International, 101*(2), 425-478.

Deng, A., and D. R. Stauffer (2006), On improving 4-km mesoscale model simulations, J. Appl. Meteorol. Climatol., 45(3), 361–381, doi:10.1175/JAM2341.1.

Dewey, J. F. and J. M. Bird (1970). "Mountain belts and new global tectonics." Journal of Geophysical Research 75(14): 2625–2647.

Dorbath, C., Gerbault, M., Carlier, G., & Guiraud, M. (2008). Double seismic zone of the Nazca plate in northern Chile: High-resolution velocity structure, petrological implications, and thermomechanical modeling. *Geochemistry Geophysics Geosystems, 9.* <Go to ISI>://WOS:000257737700002

Ekstrom, G., Nettles, M., & Dziewonski, A. M. (2012). The global CMT project 2004-2010: Centroid-moment tensors for 13,017 earthquakes. *Physics of the Earth and Planetary Interiors, 200,* 1-9. <Go to ISI>://WOS:000306047200001

Engdahl, E. R., R. van der Hilst, and R. Buland (1998), Global teleseismic earthquake relocation with improved travel times and procedures for depth determination, *B Seismol Soc Am, 88*(3), 722-743

Faccenda, M., Gerya, T. V., & Burlini, L. (2009). Deep slab hydration induced by bending-related variations in tectonic pressure. *Nature Geoscience, 2*(11), 790-793. <Go to ISI>://WOS:000271388500024

Faccenda, M., Gerya, T. V., Mancktelow, N. S., & Moresi, L. (2012). Fluid flow during slab unbending and dehydration: Implications for intermediate-depth seismicity, slab weakening and deep water recycling. *Geochemistry Geophysics Geosystems, 13.* <Go to ISI>://WOS:000299392700002

Fan, G., J. F. Ni, et al. (1994). "Active tectonics of the Pamirs and Karakoram." J. Geophys. Res. 99: 7131–7160

Fan, G., T. C. Wallace, et al. (1998). "Tomographic imaging of deep velocity structure beneath the eastern andsouthern Carpathians, Romania: Implications for continental collision." J. Geophys. Res. 103: 2705–2724

Fay, M. P., M. A. Proschan. (2010). Wilcoxon-Mann-Whitney or t-test? On assumptions for hypothesis tests and multiple interpretations of decision rules." Statistics surveys 4, 1

Ferrand, T. P., Hilairet, N., Incel, S., Deldicque, D., Labrousse, L., Gasc, J., ... Schubnel, A. (2017). Dehydration-driven stress transfer triggers intermediate-depth earthquakes. Nature Communications, 8, 15247. https://doi.org/10.1038/ncomms15247

Florez, M. A., & Prieto, G. A. (2017). Precise relative earthquake depth determination using array processing techniques Journal of Geophysical Research: Solid Earth Volume 122, Issue 6. *Journal of Geophysical Research: Solid Earth, 122*(6), 4559-4571. Retrieved from http://onlinelibrary.wiley.com/doi/10.1002/2017JB014132/abstract

Frohlich, C. (1979), EFFICIENT METHOD FOR JOINT HYPOCENTER DETERMINATION FOR LARGE GROUPS OF EARTHQUAKES, *Computers & Geosciences, 5*(3-4), 387-389, doi:10.1016/0098-3004(79)90034-7

Frohlich, C. (1989). "The nature of deep-focus earthquakes." Ann. Rev. Earth Planet. Sci. 17: 227-254.

Frohlich, C. (2006). Deep Earthquakes. Cambridge, Cambridge University Press.

Fuchs, K., K. P. Bonjer, et al. (1979). "The Romanian Earthquake of March 4, 1977: II

Aftershocks and Migration of Seismic Activity." Tectonophysics 53: 225–247

Gansser, A. (1966). "The Indian Ocean and the Himalayas a geological interpretation." Eclogae Geol.Helv., 59: 831-848

Gansser, A. (1977). "The great suture zone between Himalaya and Tibet - A preliminary account, in Himalaya." Sciences de la Terre 209-212

Green, H. W. and H. Houston (1995). "The mechanics of deep earthquakes." Ann. Rev. Earth and Planet Sci. 23: 169-213

Green, H. W., 2nd, Chen, W. P., & Brudzinski, M. R. (2010). Seismic evidence of negligible water carried below 400-km depth in subducting lithosphere. *Nature, 467*(7317), 828-831. https://www.ncbi.nlm.nih.gov/pubmed/20927105

Griggs, D. T. and J. H. Handin (1960). "Observations on fracture and a hypothesis of earthquakes. In Rock Deformation." Mem. Geol. Soc. Am. 79: 347-373

Hamburger, M. W., D. R. Sarewitz, et al. (1992). "Structural and seismic evidence for intracontinental subduction in the Peter the First range, central Asia." Geol. Soc. Am. Bull. 104: 397-408

Hacker, B. R., S. M. Peacock, G. A. Abers, and S. D. Holloway (2003), Subduction factory 2. Are intermediate-depth earthquakes in subducting slabs linked to metamorphic dehydration reactions? Journal of Geophysical Research: Solid Earth (1978?2012) Volume 108, Issue B1, *Journal of Geophysical Research: Solid Earth (1978?2012), 108*(B1), n/a

Hasegawa, A., & Nakajima, J. (2017). Seismic imaging of slab metamorphism and genesis of intermediate-depth intraslab earthquakes. *Progress in Earth and Planetary Science, 4.* <Go to ISI>://WOS:000398667500001

Hasegawa, A., Umino, N., & Takagi, A. (1978). Double-planed structure of the deep seismic zone in the northeastern Japan arc. *Tectonophysics, 47*(1), 43-58. http://www.sciencedirect.com/science/article/pii/0040195178901506

Hayes, G. P., Wald, D. J., & Johnson, R. L. (2012). Slab1.0: A three-dimensional model of global subduction zone geometries. Journal of Geophysical Research, 117, B01302. https://doi.org/10.1029/2011JB008524

Higgs, R. (2009). "Caribbean-South America oblique collision model revised." Geol.Soc. London, Spec. Pub. 328: 613-657

Hilairet, N., Reynard, B., Wang, Y. B., Daniel, I., Merkel, S., Nishiyama, N., & Petitgirard, S. (2007). High-pressure creep of serpentine, interseismic deformation, and initiation of subduction. *Science, 318*(5858), 1910-1913. <Go to ISI>://WOS:000251786600055

Hobbs, B. E. and A. Ord (1988). "Plastic instabilities: Implications for the origin of intermediate and deep focus earthquakes." J. Geophys. Res. 93: 10,521-510,540

Houston, H. (2007). "Deep earthquakes, in: G. Schubert (Ed.)." Treatise on Geophysics. Elsevier, Amsterdam: 321–350

Jiricek, R. (1979). "Tectogenetic development of the Carpathian arc in the Oligocene and Neogene, in Tectonic profiles through the West Carpathians." Geol. Inst. D. Stur: 2003–2214

John, T., M. S., et al. (2009). "Generation of intermediate-depth earthquakes by self-localizing thermal runaway." Nature Geoscience 2: 137-140

John, T. and V. Schenk (2006). "Interrelations between intermediate-depth earthquakes and fluid flow within subducting oceanic plates: Constraints from eclogite-faciespseudotachylytes." Geology 34: 557-560

Jung, H., H. W. Green, et al. (2004). "Intermediate-depth earthquake faulting by dehydration embrittlement with negative volume change " Nature Geoscience 428: 545-549

Katsumata, K. (2006). Imaging the high b-value anomalies within the subducting Pacific plate in the Hokkaido corner. *Earth Planets and Space, 58*(12), E49-E52. <Go to ISI>://WOS:000244424900034

Kearey, P. and F. Vine (1996). Global Tectonics, Blackwell Science.

Kelemen, P. B., & Hirth, G. (2007). A periodic shear-heating mechanism for intermediate-depth earthquakes in the mantle. *Nature, 446*(7137), 787-790. <Go to ISI>://WOS:000245626800038

Kennett, B. L. N., & Engdahl, E. R. (1991). Traveltimes for global earthquake location and phase identification. *Geophysical Journal International, 105*(2), 429-465. http://gji.oxfordjournals.org/content/105/2/429.abstract

Kennett, B. L. N., E. R. Engdahl, and R. Buland (1995), Constraints on seismic velocities in the Earth from traveltimes, *Geophysical Journal International*, *122*(1), 108-124, doi:10.1111/j.1365-246X.1995.tb03540.x

Kirby, S. (1995). Interslab earthquakes and phase changes in subducting lithosphere. *Reviews of Geophysics, 33*(S1), 287-297. https://doi.org/10.1029/95RG00353

Kirby, S., S. Stein, et al. (1996a). "Metastable mantle phase transformations and deep earthquakes in subducting oceanic lithosphere." Rev. Geophysics 34(2): 261-306

Kirby, S. H., E. R. Engdahl, et al. (1996b). "Intraslab earthquakes and arc volcanism: dual physical expressions of crustal and uppermost mantle metamorphism in subducting slabs, in Bebout." American Geophysical Union, Geophysical Monograph 96: 195214

Kita, S. and Ferrand T. P. (2018). Physical mechanisms of oceanic mantle earthquakes: Comparison of natural and experimental events. Scientific Reports, 8, 17049

Kita, S., Okada, T., Hasegawa, A., Nakajima, J., & Matsuzawa, T. (2010). Existence of interplane earthquakes and neutral stress boundary between the upper and lower planes of the double seismic zone beneath Tohoku and Hokkaido, northeastern Japan. *Tectonophysics,* *496*(1), 68-82. http://www.sciencedirect.com/science/article/pii/S0040195110004439

Koch, M. (1985). "Nonlinear inversion of local seismic travel times for the simultaneous determination of the 3D-velocity structure and hypocenters—Application to the seismic zone Vrancea." J. Geophys. 56: 160–173.

Koulakov, I., B. Zaharia, et al. (2010). "Delamination or slab detachment beneath Vrancea? New arguments from local earthquake tomography." Geochem.Geophys. Geosyst. 10(Q03002)

Korenaga, J. (2013), Stacking with dual bootstrap resampling, *Geophysical Journal International*, *195*(3), 2023-2036, doi:10.1093/gji/ggt373

Korenaga, J. (2017). On the extent of mantle hydration caused by plate bending. *Earth and Planetary Science Letters, 457*, 1-9. <Go to ISI>://WOS:000389398000001

Lin, G., and P. Shearer (2005), Tests of relative earthquake location techniques using synthetic data Journal of Geophysical Research: Solid Earth (1978?2012) Volume 110, Issue B4, *Journal of Geophysical Research: Solid Earth (1978?2012), 110*(B4), n/a

Linzer, H. G. (1996). "Kinematics of retreating subduction along the Carpathian arc, Romania." Geology 24: 167–170

Lorenz, F. P., M. Martin, et al. (1997). "Teleseismic travel-time tomography of the compressional-wave velocity structure in the Vrancea zone." Romania, Eos Trans. AGU 78(46)

Ma, S., and D. W. Eaton (2011), Combining double-difference relocation with regional depth-phase modelling to improve hypocentre accuracy, *Geophysical Journal International, 185*(2), 871-889, doi:10.1111/j.1365-246X.2011.04972.x

Magistrale, H., and C. Sanders (1996), Evidence from precise earthquake hypocenters for segmentation of the San Andreas Fault in San Gorgonio Pass Journal of Geophysical Research: Solid Earth (1978?2012) Volume 101, Issue B2, *Journal of Geophysical Research: Solid Earth (1978?2012), 101*(B2), 3031-3044

Martin, M., F. Wenzel, et al. (2006). "High-resolution teleseismic body wave tomography beneath SE-Romania-II. Imaging of a slab detachment scenario." Geophys. J. Int. 164: 579-595

Meade, C. and R. Jeanloz (1991). "Deep-focus earthquakes and recycling of water into the Earth's mantle." Science 252: 68-72

McGuire, J. J., & Wiens, D. A. (1995). A double seismic zone in New Britain and the morphology of the Solomon Plate at intermediate depths Geophysical Research Letters Volume 22, Issue 15. *Geophysical Research Letters, 22*(15), 1965-1968. Retrieved from http://onlinelibrary.wiley.com/doi/10.1029/95GL01806/abstract

Nishikawa, T., & Ide, S. (2014). Earthquake size distribution in subduction zones linked to slab buoyancy. *Nature Geoscience, 7*(12), 904-908. <Go to ISI>://WOS:000345915300021

Nowroozi, A. A. (1971). "Seismo-tectonics of the Persian Plateau, Eastern Turkey, Caucasus, and Hindu Kush regions." Bull. Seism. Soc. Am. 61: 317–341

Ohuchi, T., Lei, X. L., Ohfuji, H., Higo, Y. J., Tange, Y., Sakai, T., et al. (2017). Intermediate-depth earthquakes linked to localized heating in dunite and harzburgite. *Nature Geoscience, 10*(10), 771-+. <Go to ISI>://WOS:000412102200015

Okazaki, K., & Hirth, G. (2016). Dehydration of lawsonite could directly trigger earthquakes in subducting oceanic crust. *Nature, 530*(7588), 81-+. <Go to ISI>://WOS:000369304500036

Ogawa, M. (1987). "Shear instability in a viscoelastic material as the cause of deep focus earthquakes." J. Geophys. Res. 92: 13801-13810

Ojeda, A. and J. Havskov (2001). "Crustal structure and local seismicity in Colombia." J. Seismol. 5: 575-593

Oncescu, M. C. (1982). "Velocity structure of the Vrancea region, Romania." Tectonophysics 90: 117-122

Oncescu, M. C. (1984). "Deep structure of the Vrancea region, Roumania, inferred from simultaneous inversion for hypocenters and 3-D velocity structure." Ann. Geophys. 2(1): 23-28

Oncescu, M. C., K. P. Bonjer, et al. (1999). Weak and strong ground motion of intermediate-depth earthquakes from the Vrancea region in Vrancea Earthquakes: Tectonics, Hazard and Risk Mitigation. F. Wenzel, D. Lungu, O. Novak and Springer. New York: 27-42

Oncescu, M. C. and C. I. Trifu (1987). "Depth variation of moment tensor principal axes in Vrancea (Romania) seismic region." Ann. Geophys. 5B: 149–154

Oncken, O., et al. (1999), Seismic reflection image revealing offset of Andean subduction-zone earthquake locations into oceanic mantle, *Nature, 397*(6717), 341-344

Oth, A., D. Bindi, et al. (2008). "S-wave attenuation characteristics beneath the Vrancea region in Romania: new insights from the inversion of ground motion spectra." Bull. Seismol. Soc. Am. 98(5): 2482-2497

Pacheco, J. F., Scholz, C. H., & Sykes, L. R. (1992). Changes in frequency–size relationship from small to large earthquakes. Nature, 355(6355), 71

Paternoster, R., Brame, R., Mazerolle, P., & Piquero, A. (1998). Using the correct statistical test for the equality of regression coefficients. Criminology, 36(4), 859-866

Pavlis, G. L., and J. R. Booker (1980), The mixed discrete-continuous inverse problem Application to the simultaneous determination of earthquake hypocenters and velocity structure, Journal of Geophysical Research: Solid Earth (1978?2012) Volume 85, Issue B9, *Journal of Geophysical Research: Solid Earth (1978?2012)*, *85*(B9), 4801-4810

Pavlis, G. L. and S. Das (2000). "The Pamir-Hindu Kush seismic zone as astrain marker for flow in the upper mantle." Tectonics 19: 103–115

Peacock, S. M. and K. Wang (1999). "Seismic consequences of warm versus cool subduction metamorphism: Examples from southwest and northeast Japan." Science 286: 937–939

Pècskay, Z., J. Lexa, et al. (1995). "Space and time distribution of Neogene-Quaternary volcanism in the Carpatho-Pannonian region." Acta Vulcanol. 7(2): 15-28

Pegler, G. and S. Das (1998). "An enhanced image of the Pamir-Hindu Kush seismic zone from relocated earthquake hypocenters." Geophys. J. Int. 134 573-595

Penington, W. D. (1981). "Subduction of the eastern Panama basin and seismotectonics of northwestern South America " J. Geophys.Res. 86: 10,579-510,597

Pennington, W. D., W. D. Mooney, et al. (1979). "Results of a reconnaissance microearthquake survey of Bucaramanga, Colombia." Geophys. Res. Lett. 6: 6568

Pindell, J. L. and L. Kennan (2009). "South America in the mantle reference frame:

an update Tectonic evolution of the Gulf of Mexico, Caribbean and northern South America in the mantle reference frame: an update." Geol. Soc. London, Spec.Pub. 328: 1-35

Popa, M., E. Kissling, et al. (2001). "Local source tomography using body waves to deduce aminimum 1D velocity model for the Vrancea (Romania) zone." Rom. Rep. Phys. 53: 519–536

Prieto, G. A., D. J. Thomson, F. L. Vernon, P. M. Shearer, and R. L. Parker (2007), Confidence intervals for earthquake source parameters, *Geophysical Journal International*, *168*(3), 1227-1234, doi:10.1111/j.1365-246X.2006.03257.x

Prieto, G. A., Beroza, G. C., Barrett, S. A., López, G. A., & Florez, M. (2012). Earthquake nests as natural laboratories for the study of intermediate-depth earthquake mechanics. Tectonophysics, 570, 42-56

Peacock, S. M. (2001). Are the lower planes of double seismic zones caused by serpentine dehydration in subducting oceanic mantle? *Geology*, *29*(4), 299-302. http://dx.doi.org/10.1130/0091-7613(2001)029<0299:ATLPOD>2.0.CO;2

Proctor, B., & Hirth, G. (2015). Role of pore fluid pressure on transient strength changes and fabric development during serpentine dehration at mantle conditions: Implications for subduction-zone seismicity. *Earth and Planetary Science Letters, 421*, 1-12. <Go to ISI>://WOS:000355037300001

Ramirez, J. E. (2004). Actualización de la historia de los terremotos en Colombia.Instituto Geofísico Universidad Javeriana. Bogotá, D. C., Pontificia Universidad Javeriana

Ranero, C. R., Morgan, J. P., McIntosh, K., & Reichert, C. (2003). Bending-related faulting and mantle serpentinization at the Middle America trench. *Nature, 425*(6956), 367-373. <Go to ISI>://WOS:000185502300032

Reynard, B., Nakajima, J., & Kawakatsu, H. (2010). Earthquakes and plastic deformation of anhydrous slab mantle in double Wadati-Benioff zones. *Geophysical Research Letters, 37*(24). https://doi.org/10.1029/2010GL045494

Richards-Dinger, K. B., and P. M. Shearer (2000), Earthquake locations in southern California obtained using source-specific station terms, *J Geophys Res-Sol Ea*, *105*(B5), 10939-10960, doi:Doi 10.1029/2000jb900014

Rietbrock, A., and F. Waldhauser (2004), A narrowly spaced double-seismic zone in the subducting Nazca plate, *Geophysical Research Letters*, *31*(10), doi:Artn L1060810.1029/2004gl019610

Rost, S., and C. Thomas (2002), Array seismology: Methods and applications, *Rev Geophys*, *40*(3), doi:Artn 100810.1029/2000rg000100

Santo, T. (1969b). "Regional study on the characteristic seismicity of the world, I, Hindu Kush region." Bull. Earthquake Res. Inst., Tokyo Univ. 47: 1035–1049

Schaff, D. P., G. H. R. Bokelmann, G. C. Beroza, F. Waldhauser, and W. L. Ellsworth (2002), High-resolution image of Calaveras Fault seismicity, *J Geophys Res-Sol Ea, 107*(B9), doi:Artn 218610.1029/2001jb000633

Schaff, D. P., G. H. R. Bokelmann, W. L. Ellsworth, E. Zanzerkia, F. Waldhauser, and G. C. Beroza (2004), Optimizing correlation techniques for improved earthquake location, *B Seismol Soc Am, 94*(2), 705-721, doi:Doi 10.1785/0120020238

Schneider, J. F., W. D. Pennington, et al. (1987). "Microseismicity and focal mechanisms of the intermediate-depth Bucaramanga Nest, Colombia." J. Geophys. Res. 92: 13913–13926

Schimmel, M., and H. Paulssen (1997), Noise reduction and detection of weak, coherent signals through phase-weighted stacks, *Geophysical Journal International, 130*(2), 497-505, doi:DOI 10.1111/j.1365-246X.1997.tb05664.x

Shewchuk, J. R. (1994), An Introduction to the Conjugate Gradient Method Without the Agonizing Pain*Rep.*, Carnegie Mellon University

Scambelluri, M., Pennacchioni G., Gilio M., Bestmann, M., Plümper O. and Nestola, F. (2017). Fossil intermediate-depth earthquakes in subducting slabs linked to differential stress release. Nature Geoscience 10, 960–96

Schlaphorst, D., Kendall, J. M., Collier, J. S., Verdon, J. P., Blundy, J., Baptie, B., et al. (2016). Water, oceanic fracture zones and the lubrication of subducting plate boundaries-insights from seismicity. *Geophysical Journal International, 204*(3), 1405-1420. <Go to ISI>://WOS:000373719100001

Shearer, P. M. (1997). Improving local earthquake locations using the L1 norm and waveform cross correlation: Application to the Whittier Narrows, California, aftershock sequence

Shih, X. R., J. F. Schneider, et al. (1991b). "Polarities of P and S waves, and shear wave splitting observed from the Bucaramanga Nest, Colombia." J. Geophys. Res. 96: 12069-12082

Sperner, B., F. Lorenz, et al. (2001). "Slab breakoff—Abrupt cut or gradual detachment? New insights from Vrancea Region (SECarpathians, Romania)." Terra Nova 13: 172–179

Sperner, B., L. Ratschbacher, et al. (2002). "Interplay between subduction retreat and lateral extrusion: tectonics of the Western Carpathians." Tectonics 21(6): 1051. Stampfli, G. M. and G. D. Borel (2002). "A plate tectonic model for the Paleozoic and Mesozoic constrained by dynamic plate boundaries and restored synthetic oceanic isochrons." Earth and Planetary Science Letters 196 (1–2): 17–33

Suter, F., M. Sartori, et al. (2008). "Structural imprints at the front of the Choco-Panama indenter." Tectonophysics 460: 134-157

Journal of Geophysical Research-Solid Earth, 102(B4), 8269-8283. <Go to ISI>://WOS:A1997WU87600045

Sun, G., Ranson, K. J., Kimes, D. S., Blair, J. B., & Kovacs, K. (2008). Forest vertical structure from GLAS: An evaluation using LVIS and SRTM data. Remote Sensing of Environment, 112(1), 107-117

Syracuse, E. M., Abers, G. A., Fischer, K., MacKenzie, L., Rychert, C., Protti, M., et al. (2008). Seismic tomography and earthquake locations in the Nicaraguan and Costa Rican upper mantle. *Geochemistry Geophysics Geosystems, 9.* <Go to ISI>://WOS:000258147900001

Syracuse, E. M., van Keken, P. E., & Abers, G. A. (2010). The global range of subduction zone thermal models. *Physics of the Earth and Planetary Interiors, 183*(1), 73-90. http://www.sciencedirect.com/science/article/pii/S0031920110000300

Szakacs, A. and I. Seghedi (1995). "Time-space evolution of Neogene-Quarternary volcanism in the Calimani-Gurghiu-Harghita volcanic chain." Rom. J. Strat. 76(4)

Taboada, A., L. A. Rivera, et al. (2000). "Geodynamics of the northern Andes: Subductions and intracontinental deformation (Colombia)." Tectonics 19 (5): 787-813

Thurber, C. H. (1983), Earthquake locations and three-dimensional crustal structure in the Coyote Lake Area, central California Journal of Geophysical Research: Solid Earth (1978?2012) Volume 88, Issue B10, *Journal of Geophysical Research: Solid Earth (1978?2012), 88*(B10), 8226-8236

Tibuleac, I. M. (2014), A Method for First-Order Earthquake Depth Estimation Using Superarrays, *Seismol Res Lett, 85*(6), 1255-1264

Twardzik, C., and C. Ji (2015), The Mw7.9 2014 intraplate intermediate-depth Rat Islands earthquake and its relation to regional tectonics, *Earth and Planetary Science Letters, 431*, 26-35, doi:http://dx.doi.org/10.1016/j.epsl.2015.08.033

Trygvasson, E. and J. E. Lawson (1970). "The intermediate earthquake source near Bucaramanga, Colombia." Bull. Seismol. Soc. Am. 60: 269-276

Van der Hilst, R. and P. Mann (1994). "Tectonic implications of tomographic images of subducted lithosphere beneath northwestern South America." Geology 22: 451- 454

Van Stiphout, T., Kissling, E., Wiemer, S., & Ruppert, N. (2009). Magmatic processes in the Alaska subduction zone by combined 3-D b value imaging and targeted seismic tomography. *Journal of Geophysical Research-Solid Earth, 114.* <Go to ISI>://WOS:000271584500001

Waldhauser, F., and W. L. Ellsworth (2000), A Double-Difference Earthquake Location Algorithm: Method and Application to the Northern Hayward Fault, California, *B Seismol Soc Am, 90*(6), 1353-1368, doi:10.1785/0120000006

Wei, S. S., Wiens, D. A., van Keken, P. E., & Cai, C. (2017). Slab temperature controls on the Tonga double seismic zone and slab mantle dehydration. *Science Advances, 3*

Wiemer, S., & Benoit, J. P. (1996). Mapping the B-value anomaly at 100 km depth in the Alaska and New Zealand Subduction Zones Geophysical Research Letters Volume 23, Issue 13. *Geophysical Research Letters, 23*(13), 1557-1560. Retrieved from http://onlinelibrary.wiley.com/doi/10.1029/96GL01233/abstract

Wiemer, S., & Wyss, M. (2000). Minimum magnitude of completeness in earthquake catalogs: Examples from Alaska, the western United States, and Japan. *Bulletin of the*

Seismological Society of America, 90(4), 859-869. <Go to ISI>://WOS:000089060700005

Windley, B. F. (1988). "Tectonic framework of the Himalaya, Karakoram and Tibet, and the problem of their evolution." Phil. Trans. Royal SOC London A326: 3-16

Woessner, J., & Wiemer, S. (2005). Assessing the quality of earthquake catalogues: Estimating the magnitude of completeness and its uncertainty. *Bulletin of the Seismological Society of America,* 95(2), 684-698. <Go to ISI>://WOS:000229028400022

Wortel, M. J. R. and W. Spakman (1992). "Structure and dynamics of subducted lithosphere in the Mediterranean region." Proc. K. Ned. Akad. Wet. 95: 325–347

Wyss, M., Hasegawa, A., & Nakajima, J. (2001). Source and path of magma for volcanoes in the subduction zone of northeastern Japan Geophysical Research Letters Volume 28, Issue 9. *Geophysical Research Letters,* 28(9), 1819-1822. Retrieved from http://onlinelibrary.wiley.com/doi/10.1029/2000GL012558/abstract

Yamasaki, T., and T. Seno (2003), Double seismic zone and dehydration embrittlement of the subducting slab, *J Geophys Res-Sol Ea,* 108(B4), doi:Artn 221210.1029/2002jb001918

Ye, L., T. Lay, and H. Kanamori (2014), The 23 June 2014 Mw 7.9 Rat Islands archipelago, Alaska, intermediate depth earthquake, *Geophysical Research Letters,* 41(18), 6389-6395, doi:10.1002/2014GL061153

Zarifi, Z., J. Havskov, et al. (2007). "An insight into the Bucaramanga nest." Tectonophysics 443: 93-105

Zhang, H. J., Thurber, C. H., Shelly, D., Ide, S., Beroza, G. C., & Hasegawa, A. (2004). High-resolution subducting-slab structure beneath northern Honshu, Japan, revealed by double-difference tomography. *Geology,* 32(4), 361-364. <Go to ISI>://WOS:000220553900023